Numerical investigations on the flow over cubes with rounded corners and the noise emitted

Yanan Wang[a,*], Zhiwei Hu[b], David Thompson[a]

[a] *Institute of Sound and Vibration Research, Faculty of Engineering and Physical Sciences, University of Southampton, Southampton, SO17 1BJ, United Kingdom.*

[b] *Aerodynamics and Flight Mechanics Research Group, Faculty of Engineering and Physical Sciences, University of Southampton, Southampton, SO17 1BJ, United Kingdom.*

Abstract

The effect of corner rounding on the flow past a cube is investigated numerically at different Reynolds numbers ranging from 50,000 to 200,000 using delayed detached-eddy simulation in OpenFOAM. Different corner radii from 0 to 40% of the cube length have been considered. To validate the adopted methodology, a benchmark case on the flow over a sphere with the same characteristic length is first performed. Good agreement has been achieved between the results of the benchmark and available experimental and numerical data from literature. Subsequently, features of the flow around cubes with rounded corners are investigated, including the aerodynamic coefficients, mean flow patterns and the surface pressure distribution. The relation between flow features and the aerodynamic coefficients is also analysed. In addition, the far-field noise emitted from the rounded cube is predicted using the Ffowcs William-Hawkings acoustic analogy in FLUENT. It is found that corner rounding with carefully determined radius can be an effective way to reduce the emitted noise. The minimum noise is found for a radius 1/3 of the cube side length with the lowest surface pressure fluctuations, but the sound level increases again for a further increase in corner radius to $R/L = 2/5$ due to vortex shedding.

Keywords: Corner rounding, Flow patterns, Aerodynamic noise, cube, sphere

1. Introduction

The flow around bluff bodies is an important topic due to its wide applications in engineering. Many experimental and numerical investigations have been reported on the flow around cubes, spheres and cylinders with circular or square cross-sections [1–7]. Apart from cylinders, cubes with rounded corners are also commonly adopted in practical cases. For example, the knee joint of modern single-arm pantographs used on high-speed trains closely resembles a cube with rounded corners [8]; compact cuboids are also common components in train bogies [9]. Rounding the edges of bluff bodies is an efficient way to reduce the drag caused by the flow separation [10]. The present work is

*Corresponding author

Email address: yw3n14@soton.ac.uk; ynwang.swjtu@gmail.com (Yanan Wang)

an attempt to study numerically the influence of rounded corners on the flow around a cube and also to examine the implications for the emitted noise.

The flow around cuboids and cylinders with modified corners has attracted great attention in terms of both fundamental flow physics and the effects on aerodynamics. Okamoto and Uemura [11] measured the surface pressure of wall-mounted cubes with different rounded corners in a wind tunnel at a Reynolds number of $47,400$. Based on the measured surface pressure distribution, drag coefficients were determined and analysed; vortices around the rounded cubes were visualised using the ink shedding method and velocity profiles in the near-wake were also measured using a hot-wire anemometer. Direct numerical simulations (DNS) on the flow past a square cylinder with rounded or chamfered corners at a Reynolds number of $10,000$ were conducted by Tamura et al. [12], complemented with measurements performed for the same objects at the same conditions [13]. They pointed out that even a slight change of the corner shape could lead to significant variations in flow features; the pressure near the corner decreases significantly, leading to large reductions of the drag. Zhang and Samtaney [14] also employed DNS to investigate the effect of the corner radius on the flow past an isolated square cylinder at a Reynolds number of 1,000. Five different corner radii ranging from the square to the circular cross-sections were taken into account and the development of the separated and transitional flow was studied.

Hu et al. [15] employed particle imaging velocimetry (PIV) and laser doppler anemometry to investigate the near wake of square cylinders with different rounded corners. It was found that the vortex formation length in the base region was almost doubled as the ratio of the rounding radius to the square cylinder width was increased from 0 to 0.5. The phase-averaged flow structures and the velocity profiles were also presented. Miran and Sohn [10] conducted large eddy simulations (LES) to study the effect of rounded corners on the flow around a square cylinder at a Reynolds number of 500. They found that the drag is minimised when the rounded radius is 20% of its cross section width. They also reported PIV measurements in a water tunnel to investigate the effect of rounded corners on the near-wake flow of a square cylinder at a higher Reynolds number of 5,200 [16] giving detailed flow patterns in the wake. Carassale et al. [17] carried out measurements in a wind tunnel using a force balance and pressure taps to investigate the flow characteristics around square cylinders with rounded edges for Reynolds numbers between $17,000$ and $230,000$; three corner radii were considered. It was found that the separated flow reattached to the lateral surfaces further upstream as the corner radius was increased and this affected the Strouhal number of vortex shedding.

In terms of the flow-induced noise from bluff bodies, there is little published work on cuboids, despite many studies on cylinders [18–21]. Becker et al. [22] measured the noise emitted from a forward-facing step with sharp corners in an aeroacoustic wind tunnel and numerical simulations were also performed under similar flow conditions. In their numerical work, steps with three different corner radii were considered and the correlation between the near-field pressure fluctuation and the far-field noise was analysed to characterise the noise sources. Awasthi et al. carried out measurements on the pressure fluctuations of forward-facing steps with different corner radii immersed in a turbulent boundary layer [23], and also conducted measurements and predictions of the far-field noise from these steps [24]. Four corner radii from 0 to 0.25 of the step height were considered at Reynolds numbers ranging from $35,000$ to $104,000$. It was found that the pressure on the step surface scaled with the step height and the flow speed; the emitted noise reduced with the increase of the corner radius and the shape of the noise spectrum changed only slightly. In addition, Awasthi [25] also measured the sound from three-dimensional surface discontinuities represented by swept forward-facing steps with rounded corners.

As reviewed above, although several studies have been conducted to investigate the influence of rounded corners on the flow around bluff bodies, most of them are focused on square cylinders, with limited studies on the noise emitted. The present work focuses on a more compact body, namely a cube, where highly three-dimensional flow is expected. This work is intended to characterize the effect of corner rounding on the flow patterns around a cube and also the implications for the emitted noise. Numerical simulations to obtain the flow features are performed with the open source software package OpenFOAM using DDES as the turbulent modelling approach. Based on the surface pressure fluctuations sampled in the OpenFOAM, the far-field noise is subsequently predicted using the Ffowcs Williams-Hawkings (FW-H) acoustic analogy in the commercial software FLUENT, since that is not embedded in the adopted version 2.4.0 of OpenFOAM. This approach has the advantage that the number of processors that can be used is not limited by the software licence. To predict the noise in FLUENT, the OpenFOAM mesh is firstly converted to be recognizable to FLUENT using the utility $foamMeshToFluent$. The sampled pressure from OpenFOAM is then sorted by the coordinates of the cells and written into the asd format file used in FLUENT for the FW-H acoustic analogy.

2. Numerical method

2.1. Governing equations

At low Mach numbers (M), typically $M < 0.3$ [26], the flow can be assumed for most purposes to be incompressible. The governing equations for incompressible flow are as follows, in which the flow density ρ is treated as constant [27],

$$\frac{\partial u_j}{\partial x_j} = 0 \tag{1}$$

$$\frac{\partial u_i}{\partial t} + u_j \frac{\partial u_i}{\partial x_j} = -\frac{1}{\rho}\frac{\partial p}{\partial x_i} + \nu \frac{\partial^2 u_i}{\partial x_j^2} \tag{2}$$

where t is the time, p is the pressure, u_i are velocity components along the coordinate directions x_i (i=1, 2, 3) and ν is the kinematic viscosity.

Since these equations can hardly be solved analytically, turbulence models are used to find the solutions numerically. Approaches, such as Reynolds-averaged Navier-Stokes (RANS), LES and DNS, provide different levels of fidelity in Computational Fluid Dynamics (CFD) studies with different mesh requirements. The detached-eddy simulation (DES) is a hybrid RANS-LES model originally proposed by Spalart et al. [28, 29], based on the one-equation Spalart-Allmaras (S-A) RANS model. This methodology employs RANS near solid boundaries within the attached boundary layer and changes to LES outside the boundary layer. It can deal practically with separated flow at high Reynolds numbers, balancing the resolution of flow details and the computational cost. By adopting RANS in the near-wall region, the mesh resolution required by DES in this region is much less demanding than LES. The delayed DES (DDES) was subsequently proposed [30] to address some inherent flaws in DES, such as Modelled Stress Depletion [31] and Grid Induced Separation [32]. In addition to the DES based on the S-A model, Travin et al. [33] proposed a DES model adapted from the two-equation $k - w - SST$ model. The $\overline{v^2} - f$ RANS model is also studied extensively [34–36], due to its capability in predicting flow features close to the wall. Mirzaei and Sohankar [37] developed a DES model based on the $k-\omega-\overline{v^2}-f$ model and illustrated its success in predicting the flow through plane and wavy channels and over two adjacent square cylinders. A more comprehensive review of the hybrid turbulence model can be found in the literature [31]. In this work, the DDES based on the default S-A model in OpenFOAM is used to obtain the flow characteristics, which is capable to resolve the viscous sublayer

[38]. Detailed descriptions of this method were presented in [39]. The feasibility of this model in describing the flow over bluff bodies is illustrated in the following Section 4.

2.2. Ffowcs Williams-Hawkings acoustic analogy

In principle, the radiated acoustic waves can be obtained by solving the unsteady compressible Navier-Stokes (N-S) equations directly using very large computational domains. However, it is hardly achievable for applications at Reynolds numbers of industrial interest. Lighthill [40, 41] rearranged the compressible N-S equations to describe the sound generated by a region of turbulent flow in a stationary fluid [42]. The Lighthill acoustic analogy determines the equation of sound wave propagation to the far-field, distinct from the flow motion. Ffowcs Williams and Hawkings [43] further developed the acoustic analogy theory proposed by Lighthill, taking into account the presence of solid boundaries in the flow. The sound radiation is calculated for free propagation outside the solid surface. It consists of a classical wave operator on the left-hand side and a set of equivalent sources on the right-hand side, as follows:

$$\frac{1}{c_0^2}\frac{\partial^2[p'H(f)]}{\partial t^2} - \nabla^2[p'H(f)] = \frac{\partial^2}{\partial x_i \partial x_j}[H(f)T_{ij}] - \frac{\partial}{\partial x_i}[\delta(f)F_i] + \frac{\partial}{\partial t}[\delta(f)Q] \tag{3}$$

In Equation (3), $p'H(f)$ is the windowed pressure fluctuation, where p' represents the fluctuating pressure and $H(f)$ is the Heaviside function, which equals 1 outside the FW-H surface ($f > 0$), and zero elsewhere ($f \leq 0$). T_{ij}, F_i and Q are the equivalent quadrupole, dipole and monopole sources respectively (more details can be found in [43]). The Dirac delta function $\delta(f)$ indicates that the mass oscillation (Q) and the force source (F_i) are only present on the control surface defined by $f = 0$.

3. Computational setup

A two-dimensional sketch of the computational domain in the $z = 0$ plane, together with the assigned boundary conditions, is illustrated in Fig. 1(a). Those in the $y = 0$ plane are identical due to symmetry. The origin of the coordinate system is located at the cube centre and the $x-$, $y-$, $z-$ axes represent the streamwise, cross-flow (vertical) and spanwise (lateral) directions respectively. The cube has dimensions $L = 75$ mm and is rounded at all edges with a radius R. Five different corner radii are taken into account: $R/L = 0$, 1/12, 1/6, 1/3 and 2/5. The free-stream velocities of the incident flow considered are $U_\infty = 10$, 15, 20, 30 and 40 m/s. The corresponding Reynolds numbers are $Re = 50,000$, $75,000$, $100,000$, $150,000$ and $200,000$, respectively. The overall size of the

computational domain is $26L \times 13L \times 13L$, giving a maximum blockage ratio 0.6%, which is smaller than the 3% recommended by Franke et al. [44]. $Velocity\,Inlet$ and $Pressure\,Outlet$ boundaries are adopted in the simulation, as shown in Fig. 1(a). The cube surface is assigned as a $No-slip\,wall$ and $Symmetry\,Plane$ is applied to the other boundaries.

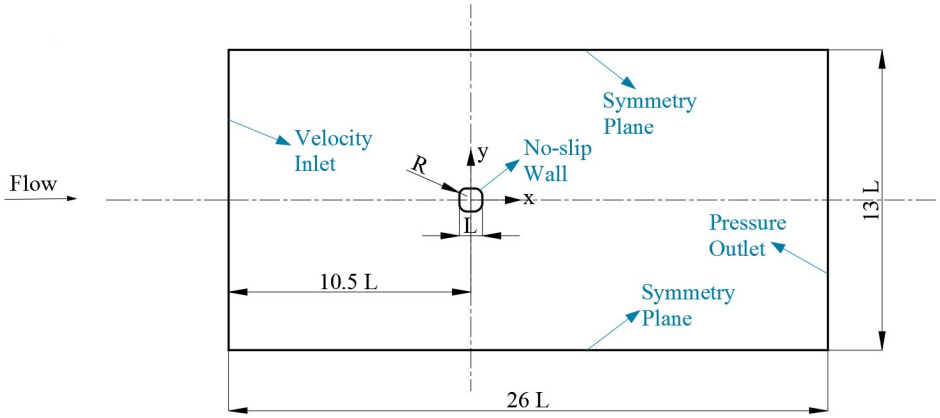

(a)

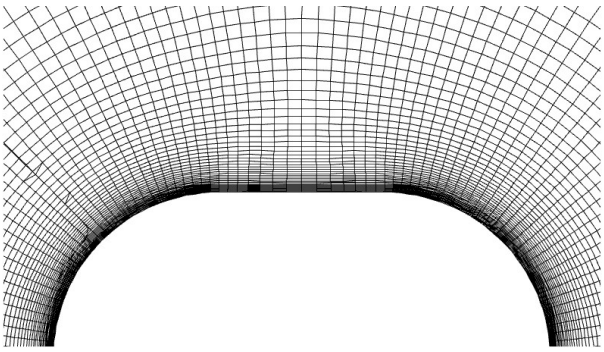

(b)

Figure 1: (a) sketch of the computational domain in the $z = 0$ plane, (b) an illustration of the near-wall mesh

Fully-structured meshes are generated for all the simulations in this work and an illustration of the mesh near the rounded cube is shown in Fig. 1(b). The grid resolution is determined based on the meshing strategy developed in a grid dependence study previously performed for flow around a wall-mounted cube [45]. The maximum dimensionless wall distance of the first layer (y_1^+) is targeted at 1.5. Based on the y_1^+, the height of the first layer cells can be calculated, which rapidly becomes smaller with increasing Reynolds number. The finest mesh resolution is applied adjacent to the cube and cells are stretched further away with a ratio about 1.09. The minimum aspect ratio of the first-layer cells is located at the rounded corners, with $\Delta x/\Delta y = \Delta z/\Delta y \approx 30$ (Δx, Δy and Δz are the grid dimensions) while the maximum aspect ratio is about 120 found in the middle of the cube edges. To capture the

flow separation well, grids on the rounded corners are evenly distributed using the smallest aspect ratio. Therefore, the total number of grid cells (N_{grid}) increases for enlarged corner radii and Reynolds numbers. A summary of the N_{grid} for the studied cases is presented in Table 1.

Re \ R/L	0	1/12	1/6	1/3	2/5	1/2
50,000	0.796	0.965	1.34	1.69	2.00	3.73
75,000	1.43	1.80	2.20	2.67	2.95	
100,000	3.15	4.21	4.66	6.12	6.99	
150,000	4.95	6.24	6.40	8.33	9.55	
200,000	8.54	10.6	11.7	19.3	22.9	

Table 1: A summary of the N_{grid} (in millions) for the studied cases

A central differencing interpolation with second-order accuracy is used as the default numerical scheme, while a Total Variation Diminishing (TVD) approach combining the central and upwind schemes is employed to calculate the divergence terms ($u_j \frac{\partial u_i}{\partial x_j}$) in the governing equations. The unsteady terms ($\frac{\partial u_i}{\partial t}$) are discretised using an implicit scheme with second-order accuracy. The simulations in this work are carried out on the iridis 4 supercomputer at the University of Southampton and are initialized from 0 s. The time step used for these simulations is 1×10^{-5} s which corresponds to maximum Courant-Friedrichs-Lewy (CFL) numbers lower than 2. About 5 physical seconds ($t^* = U_\infty * t/L \approx 667$) can be obtained during a wall time of 60 hours using 160 cores for the cube with sharp corners at $Re = 50,000$, while less than 0.05 s ($t^* \approx 27$) is calculated for the cube with $R/L = 2/5$ at $Re = 200,000$ under the same condition. In this work, the aerodynamic coefficients are calculated in the period from $t^* = 400$ to 2000 for $Re = 50,000$, 75,000 and 100,000, while t^* extends up to about 1800 for $Re = 150,000$ and 1500 for the highest Re.

4. Benchmark cases

4.1. Flow over a wall-mounted cube

To evaluate the feasibility of the adopted numerical method in predicting the flow features, a benchmark case on a wall-mounted cube placed in uniform flow was conducted and compared with experimental results at $Re = 50,000$

in [45]. Commendable agreement was achieved both quantitatively and topologically between the simulation and the measurements. In particular, the feasibility of the adopted methodology for predicting the near-wall flow patterns was validated in [45] by comparing the numerical results with the available near-wall PIV measurements. The meshing strategy adopted in the present work is derived from that used in this benchmark case.

4.2. Pressure fluctuations of a square cylinder and the far-field noise

Since no measurements of pressure fluctuations (p_{rms}) on cuboids are available in the literature for validation purposes, a separate simulation for flow over a square cylinder has been conducted using the same approach to gain confidence in the adopted methodology for predicting p_{rms}. Results were presented in [45] and a good agreement of the fluctuating pressure along the square cylinder was achieved between the numerical work and the experimental data from the literature.

To evaluate the noise prediction using the FW-H analogy, the noise emitted from a square cylinder to the far field was predicted and compared with measurements in [45]. It was found that the discrepancies between the predicted Overall Sound Pressure Level (OASPL) and the measurements at different receivers at a flow speed of 20 m/s were mostly less than 1 dB.

4.3. Flow over a sphere

For the cube with sharp corners, the flow always separates from the leading edges when the Reynolds number is greater than about $30,000$ [46–48]. However, once the sharp corners are rounded, the location of the flow separation varies. In particular, when the radius of the rounded corner is $R/L = 0.5$, the cube becomes a sphere with a diameter $D = L$. To increase confidence further in the adopted numerical methodology, especially in predicting the flow separation location, which has a strong impact on flow in the wake and surface pressure fluctuations, another benchmark case on the flow around a sphere at a Reynolds number of 50,000 is carried out and compared with the literature. A similar mesh and computational domain are used as described in Section 3 for the rounded cubes. Fig. 2 illustrates the distribution of y_1^+ on the sphere surface in the $z = 0$ plane; the position is denoted by the angle ϕ, which is measured clockwise from the front stagnation point. As shown in Fig. 2, the maximum value of y_1^+ is smaller than 1.5; the mean value of y_1^+ is 0.73.

According to the literature [49–52], the flow around a sphere changes only slightly in the Reynolds number range from $Re = 10,000$ to $300,000$. This is in the subcritical region where the boundary layer separates from the

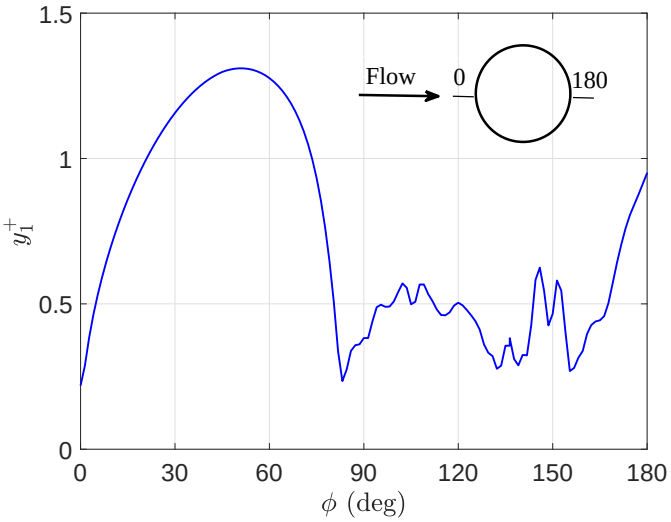

Figure 2: The distribution of y_1^+ along the sphere surface in the $z = 0$ plane

sphere surface as laminar before transition happens. Results obtained employing DDES from the current study are compared with the measurements of Achenbach [7] obtained at a Reynolds number of $162,000$, which is in the same regime. Fig. 3(a) shows the comparison of the surface pressure coefficient $C_p = (P - P_\infty)/(0.5\rho U_\infty^2)$, where P is the mean pressure on the sphere surface and $P_\infty = 0$ is the reference pressure. Fig. 3(b) shows the normalised skin friction coefficient $Re^{1/2}\tau_w/(\rho U_\infty^2)$, where τ_w is the wall shear stress.

A commendable agreement of the pressure distribution has been achieved between the simulation and the measurement as shown in Fig. 3(a), while the agreement for the skin friction in Fig. 3(b) is also reasonable. The location of the flow separation, where the skin friction first becomes zero, is captured accurately ($\phi \approx 82°$), despite the slight over-prediction of the skin friction coefficient at positions $\phi < 60°$. The probable reason for the discrepancy is the limited capability of turbulent models for transitional flow, considering the fact that the boundary layer separation from the sphere surface is laminar in the subcritical flow region [7].

Fig. 4 compares the current velocity profiles at $x/D = 0.3$ with the measurements conducted by Bakic [53] at a Reynolds number of 51,500 and the LES of Schmidt [54] at $Re = 50,000$. In Fig. 4, $\overline{U}$ and $\overline{V}$ denote mean streamwise and cross-flow velocities respectively, while the subscript rms indicates the root mean square values. The mean and rms streamwise velocities (Fig. 4(a) and 4(c)) agree well with both the measurement and the LES results. Predictions of the mean and rms cross-flow velocities (Fig. 4(b) and 4(d)) correctly capture the shape of the profiles from the literature despite slight differences in the magnitude, indicating good predictions of the separated

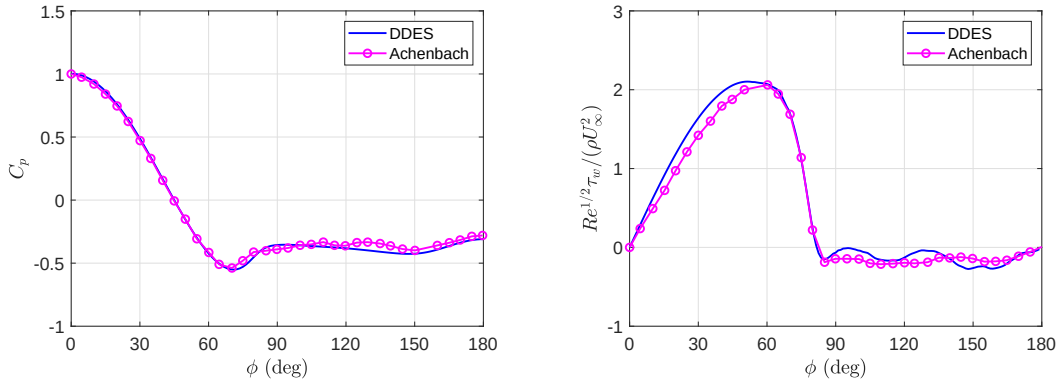

(a) Pressure distribution

(b) Skin friction distribution

Figure 3: Distributions of pressure and skin friction along the sphere surface in the $z = 0$ plane compared with the measurements from Achenbach [7]

shear layer. In addition, Fig. 5 shows mean and rms values of the streamwise velocity in the wake of the sphere at $x/D = 0.5$, 1 and 2 obtained from this work, which are compared with the literature [53, 54]. Note that in both the measurements conducted by Bakic [53] and LES simulations implemented by Schmidt [54], a string with a diameter of $d = 0.12D$ was used to support the sphere in its wake. Considering this difference in the setup, the results from the current DDES can be considered sufficiently close to the published results.

Non-dimensional aerodynamic coefficients, which reflect the overall characteristics of the flow, are defined as:

$$C_a = \frac{F_a}{0.5\rho U_\infty^2 A} \tag{4}$$

where C_a represents the drag, lift and side-force coefficients, namely, C_d, C_l and C_s respectively. F_a is the corresponding drag, lift or side force acting on the body in the x, y and z directions. ρ is the flow density and A is the frontal area; for the rounded cubes, this varies with the corner radius. The flow parameters of the sphere in cross-flow obtained from the current work are presented in Table 2 and compared with available experimental and numerical results. In Table 2, $\overline{C}_d$ is the mean drag coefficient, L_r is the length of the recirculation region in the wake, measured in the $z = 0$ plane from the rear base point of the sphere at $(0.5D, 0, 0)$ to the location where the streamwise velocity recovers to zero from negative values and $St = fD/U_\infty$ is the Strouhal number associated with the peak, where f is the peak frequency. Good agreement in terms of these statistics is achieved between this work and the literature.

As described above, distributions of the skin friction and pressure coefficients around the sphere surface, the

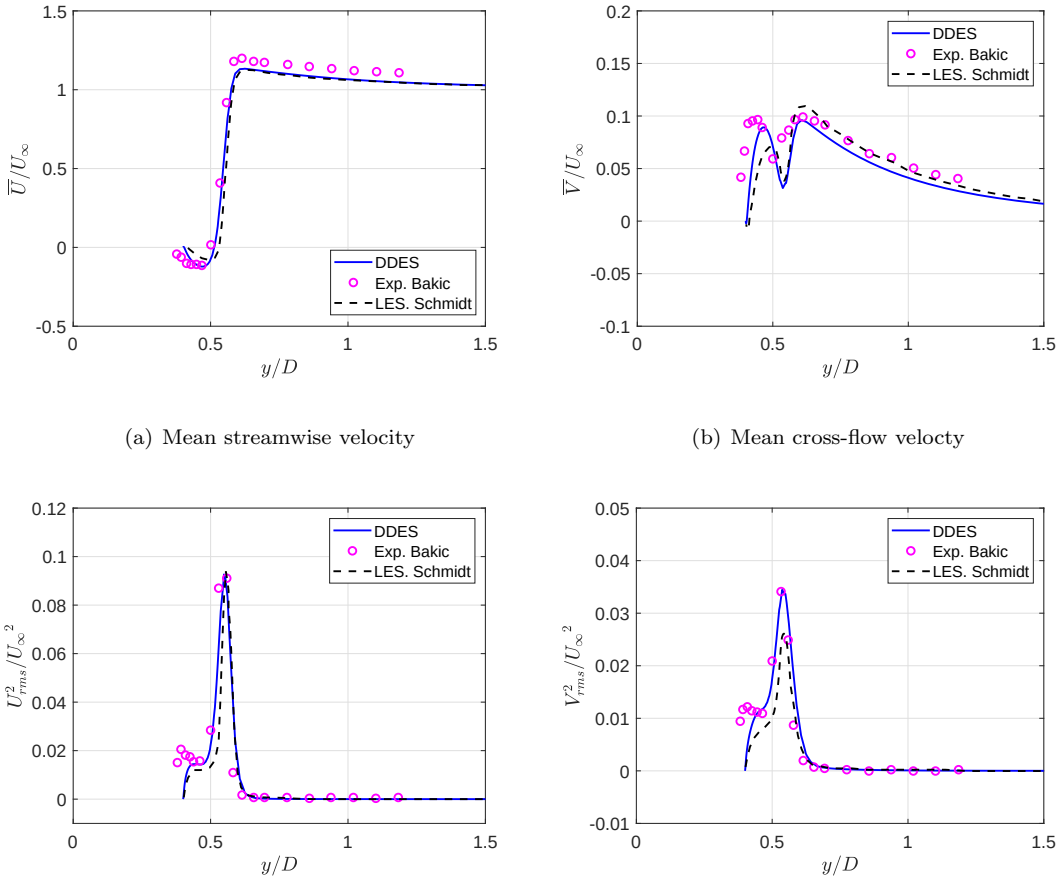

(a) Mean streamwise velocity

(b) Mean cross-flow velocty

(c) rms values of streamwise velocity

(d) rms values of cross-flow velocity

Figure 4: Velocity profiles at $x/D = 0.3$ for a sphere compared with Bakic [53] and Schmidt [54]

velocity profiles at different positions and also some key parameters describing the flow obtained from the current simulation show good agreement with data reported in the literature, which provides validation of the current DDES approach.

4.4. Additional grid dependence studies

To further validate the above described mesh resolution in addition to the benchmark case studied in reference [45], grid dependence studies are implemented for the $R/L = 1/12$ at $Re = 200,000$. The original mesh for this case is coarsened and refined respectively by a ratio of $\sqrt{2}$ to obtain the new meshes for trial. Details of the grid investigations are shown in Table 3, where N_{grid} denotes the total number of cells. The frontal area of this case is chosen as the reference area to calculate the aerodynamic coefficients and the mean lift and side-force coefficients are close to zero due to the symmetry. As can be seen from Table 3, the statistics only change slightly with the

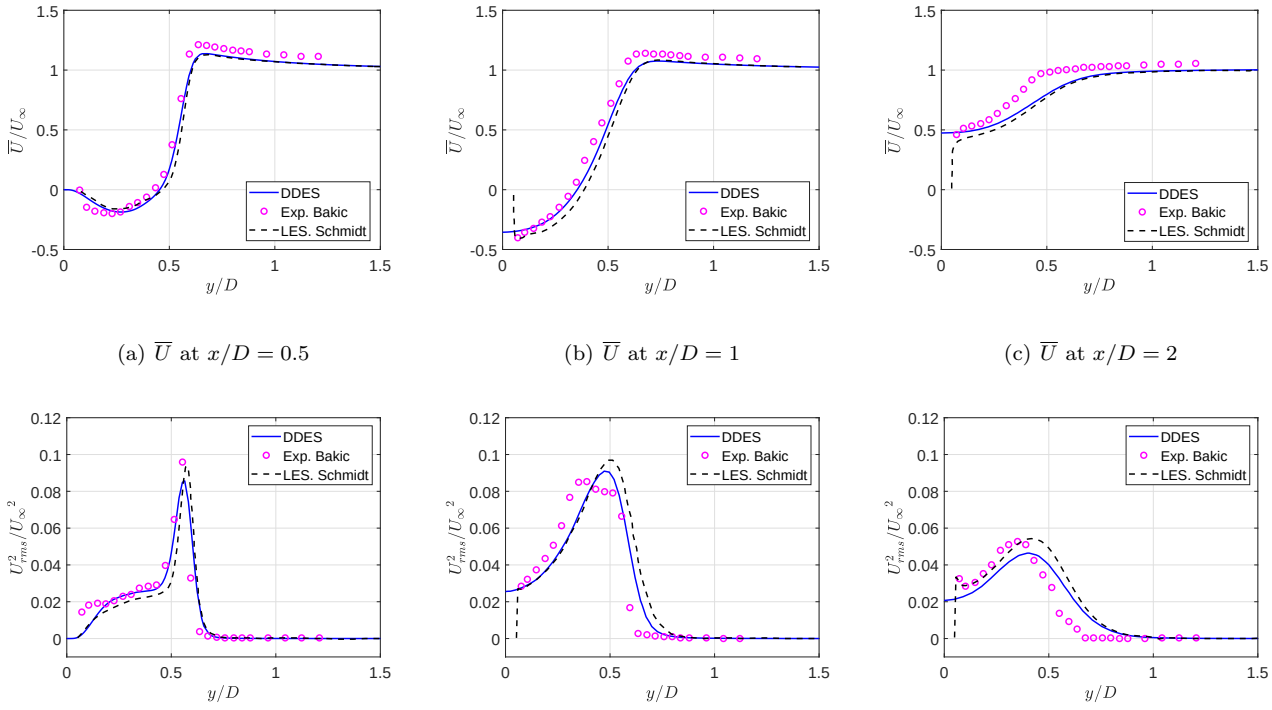

(a) $\overline{U}$ at $x/D = 0.5$ (b) $\overline{U}$ at $x/D = 1$ (c) $\overline{U}$ at $x/D = 2$

(d) U_{rms} at $x/D = 0.5$ (e) U_{rms} at $x/D = 1$ (f) U_{rms} at $x/D = 2$

Figure 5: Velocity profiles at x/D=0.5, 1 and 2 for a sphere compared with Bakic [53] and Schmidt [54]

	Method	Re	$\overline{C}_d$	L_r/D	St
Present	DDES	50,000	0.476	0.89	0.192
Achenbach [7]	Exp.	50,600	0.480		
Wieselsberger and Gersten [55]	Exp.	50,200	0.478		
Schlichting [56]	Exp.	10,000	0.4		0.195
Tomboulides [57]	LES	20,000		0.85	0.19
Constantinescu and Squires[58]	DES	100,000	0.414		
Rodríguez et al. [59]	DDES	20,000	0.411		0.198
Robertson et al. [60]	DDES	10,000	0.402		0.195

Table 2: Statistical parameters of the flow around a sphere

further refined mesh, which implies the original grid resolution is sufficient. Fig. 6 shows the distributions of the y_1^+ in the $y = 0$ plane along surfaces of the cubes with different corner radii at $Re = 200,000$. The maximum values

of the y_1^+ in Fig. 6 are smaller than 2 and the average values are well below 1.

R/L	mesh	N_{grid}	$\overline{C_d}$	$C_{\text{d},rms}$	$C_{\text{l},rms}$	$C_{\text{s},rms}$
1/12	coarse	6.39×10^6	0.4022	0.0153	0.0225	0.0236
1/12	original	1.06×10^7	0.3945	0.0129	0.0197	0.0202
1/12	refined	2.60×10^7	0.4071	0.0116	0.0209	0.0211

Table 3: Grid dependence investigations on the $R/L = 1/12$ at $Re = 200,000$

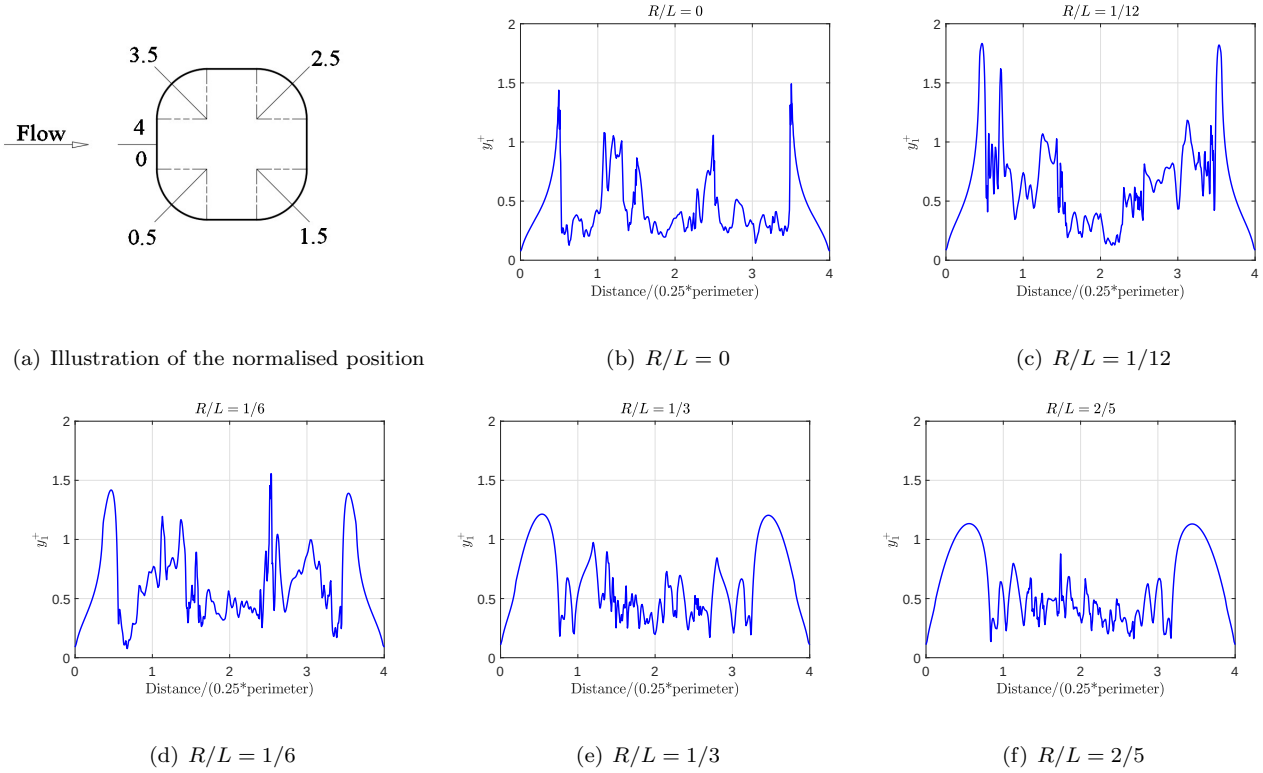

(a) Illustration of the normalised position (b) $R/L = 0$ (c) $R/L = 1/12$

(d) $R/L = 1/6$ (e) $R/L = 1/3$ (f) $R/L = 2/5$

Figure 6: Distributions of y_1^+ along the cube surfaces in the $y = 0$ plane at $Re = 200,000$

5. Flow around cubes with rounded corners

5.1. Aerodynamic coefficients

In general, each simulation was run for over 40 flow-through times ($26L/U_\infty$ in the current work) to ensure that the flow develops to a statistical steady state. This was checked by monitoring and comparing the aerodynamic coefficients averaged over every two flow-through times. The aerodynamic coefficients were collected once the variation of the values averaged in each time segment converge. Fig. 7(a) summarises the mean drag coefficients

obtained for the cube with different corner radii and different Reynolds numbers; the dashed line represents the average value over different Reynolds numbers. The calculated mean lift and side-force coefficients are very close to zero, confirming convergence of the statistics for symmetrical objects. For comparison purposes, the mean drag coefficient of the sphere obtained from the benchmark case is also shown, namely at $R/L = 1/2$. This has been obtained only at $Re = 50,000$, but the drag coefficient $\overline{C}_d$ for a sphere tends to vary very little in the studied range of Reynolds numbers [7].

As can be seen from Fig. 7(a), the values of $\overline{C}_d$ for each value of R/L at different Reynolds numbers collapse well to the trend denoted by the dashed line and the absolute differences from the average value at the studied Reynolds numbers are within 15%. The mean drag coefficient does not change monotonically with the increase of the corner radius. The lowest mean drag coefficient is observed at $R/L = 1/3$ for all the Reynolds numbers considered, while the highest value is found from the cube ($R/L = 0$). A similar trend of $\overline{C}_d$ was observed from square cylinders with different corner radii reported by Miran and Sohn [10], for which the minimum $\overline{C}_d$ was found near $R/L = 0.2$. Bearman et al. [61] measured the drag coefficients of cylinders with rounded corners in an oscillatory flow and reported the lowest $\overline{C}_d$ at $R/L = 0.265$. Here the mean drag coefficient drops significantly when the cube corners are rounded even with a small radius $R/L = 1/12$. With the increase of the radius from $L/12$ to $L/3$, the variation in the mean drag coefficient is much smaller. For radii greater than $L/3$, the drag coefficient increases slightly, although its value is still much smaller than that for the cube. The mean drag coefficient of the rounded cube with $R/L = 1/12$ is most affected by the Reynolds number.

The drag coefficient shown in Fig. 7(a) is based on the total drag, which consists of two components, namely, the pressure drag and the friction drag [27]. Fig. 7(b) illustrates the percentage of the total drag that is due to the friction drag, which is always smaller than 6%. Especially, for the cube with $R/L = 0$, this contribution is almost zero. It implies the friction drag is negligible for the studied cases. The above described variations of the mean drag coefficient are closely related with the flow characteristics, which will be analysed in the Section 5.5 below.

The dependence on the corner radius of the rms values of both the drag and lift coefficients, denoted as $C_{d,\mathrm{rms}}$ and $C_{l,\mathrm{rms}}$, is plotted in Fig. 8 using the same scales; the average values over different Reynolds numbers are shown by the dashed line. The rms values of the side-force coefficient are not displayed as they are virtually the same as those for $C_{l,\mathrm{rms}}$ due to symmetry. The values of $C_{l,\mathrm{rms}}$ are higher than those for $C_{d,\mathrm{rms}}$ in all the investigated cases. In addition, the dependence of $C_{l,\mathrm{rms}}$ on the radius R in Fig. 8(b) is much more significant than that observed for

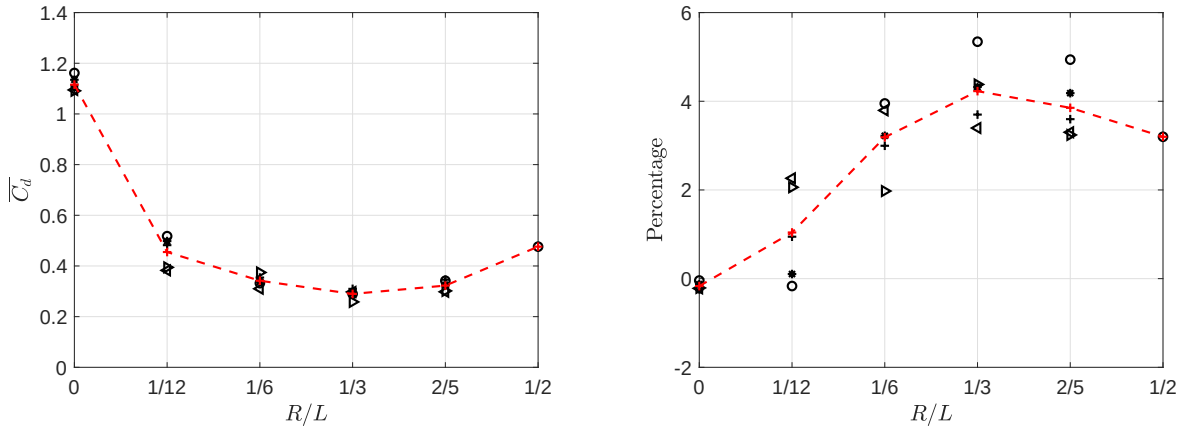

(a) The mean drag coefficient ($\overline{C}_d$)

(b) Contribution of the friction drag

Figure 7: Trends of the drag coefficient varying with the corner radius (R). ○: $Re = 50,000$; ∗: $Re = 75,000$; +: $Re = 100,000$; ◁: $Re = 150,000$; ▷: $Re = 200,000$; $-+-$: Average value

$C_{d,\mathrm{rms}}$ in Fig. 8(a). Similar to $\overline{C}_d$, the rms values of the drag and lift coefficients do not change monotonically with the corner radius. In general, the lowest value of $C_{d,\mathrm{rms}}$ is observed for $R/L = 1/3$, while the minimum value for $C_{l,\mathrm{rms}}$ is found in the case with $R/L = 1/12$. The values of both $C_{d,\mathrm{rms}}$ and $C_{l,\mathrm{rms}}$ increase significantly from $R/L = 1/3$ to $2/5$ at each investigated Re and then drop for the sphere.

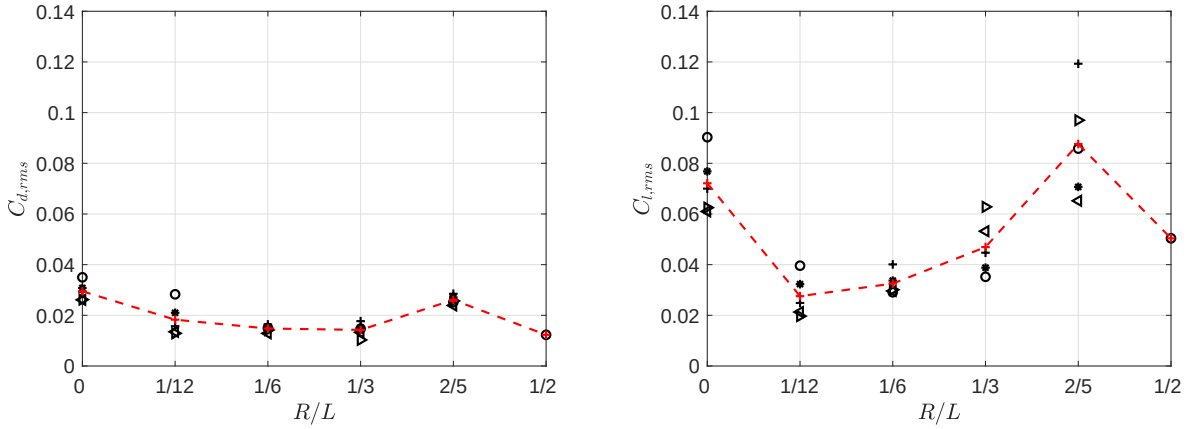

(a) $C_{d,\mathrm{rms}}$ varying with R

(b) $C_{l,\mathrm{rms}}$ varying with R

Figure 8: The trend of the root mean square values of the drag and lift coefficients varying with the corner radius (R). ○: $Re = 50,000$; ∗: $Re = 75,000$; +: $Re = 100,000$; ◁: $Re = 150,000$; ▷: $Re = 200,000$; $-+-$: Average value

As can be seen in Fig. 8, the rms values of aerodynamic coefficients are also affected by the Reynolds number. The rms values of the drag coefficient are most sensitive to the Reynolds number at $R/L = 1/12$. The values

of $C_{l,\mathrm{rms}}$ are dependent on the Reynolds number at different corner radii and change the most for the case with $R/L = 2/5$. Also for the cube with $R = 0$, the rms values of the force coefficients are more sensitive to the change of Reynolds numbers than the mean drag coefficient, which was also observed in [62]. Despite the fact that the rms values of these aerodynamic coefficients are dependent on the Reynolds number, no systematic dependence is observed.

The power spectral densities (PSDs) of the drag and lift coefficients for cubes with different corner radii are shown in Fig. 9 for $Re = 50,000$ as examples. These are calculated from the time histories of the force coefficients using Welch's method. A Hanning window is also applied. The frequency resolution in Fig. 9 is 1.5 Hz ($St = 0.011$) for the cubes with $0 \leq R/L \leq 2/5$, and 1.2 Hz ($St = 0.009$) for the sphere with $R/L = 1/2$. As can be seen from Fig. 9(a), no evident peaks are found in the spectra of C_d for Strouhal numbers smaller than 1; for Strouhal numbers above 1, the drag coefficient spectra reduce rapidly. For the PSDs of the lift coefficient given in Fig. 9(b), the spectra drop quickly at Strouhal numbers above 0.3. In addition, a broadband peak centred near $St = 0.1$ can be seen in the spectrum for the cube ($R/L = 0$), and a narrower peak centred about $St = 0.16$ is clearly seen for the rounded cube with $R/L = 2/5$. However, no evident peaks are identified for the other cases. These peaks are related with periodic vortex shedding in the wake and are the main reasons for the higher values of $C_{l,\mathrm{rms}}$ observed for the cube ($R/L = 0$) and the case with $R/L = 2/5$ in Fig. 8(b).

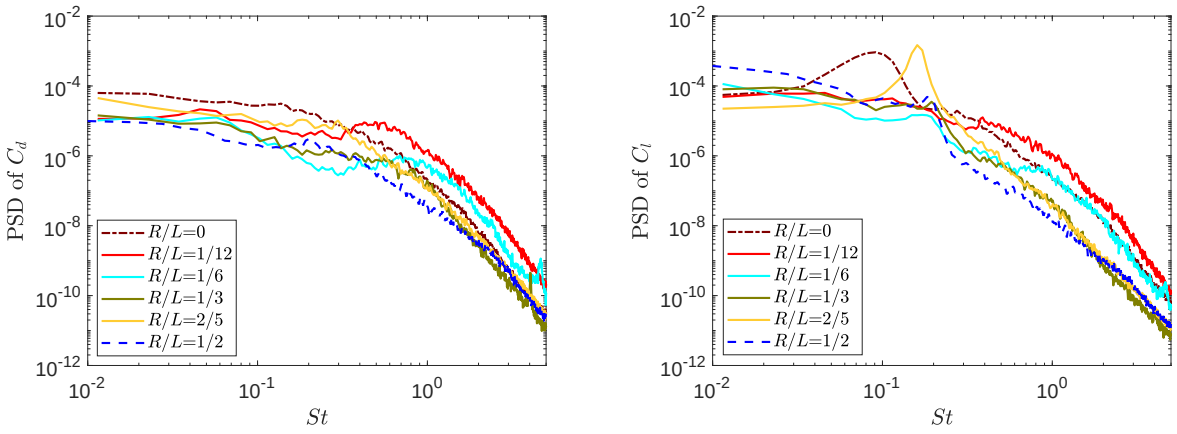

(a) PSDs of the drag coefficeint

(b) PSDs of the lift coefficeint

Figure 9: PSDs of the aerodynamic coefficients for different corner radii at $Re = 50,000$

To illustrate the Reynolds number dependence of the rms values shown in Fig. 8, PSDs of C_d for $R/L = 1/12$ at different Reynolds numbers are shown in Fig. 10(a), while the spectra of the lift coefficient for $R/L = 2/5$ are

displayed in Fig. 10(b). In Fig. 10(a), no apparent peaks can be detected and the frequency range most affected by the Reynolds number is $St \leq 1$, which is also true for cases with other corner radii (not shown). Major changes of the spectra in Fig. 10(b) for $R/L = 2/5$ mainly occur between $St = 0.05$ and 0.2, and the spectra drop rapidly when the Strouhal number exceeds 0.2. Distinct peaks centred between $St = 0.06$ and 0.16 with different amplitudes are observed at different Reynolds numbers, which explain the fluctuations of $C_{l,\mathrm{rms}}$ for $R/L = 2/5$ in Fig. 8(b). However, the distinct peaks seen in Fig. 10(b) only appear for this case with $R/L = 2/5$ and are not observed for other cases studied in this paper.

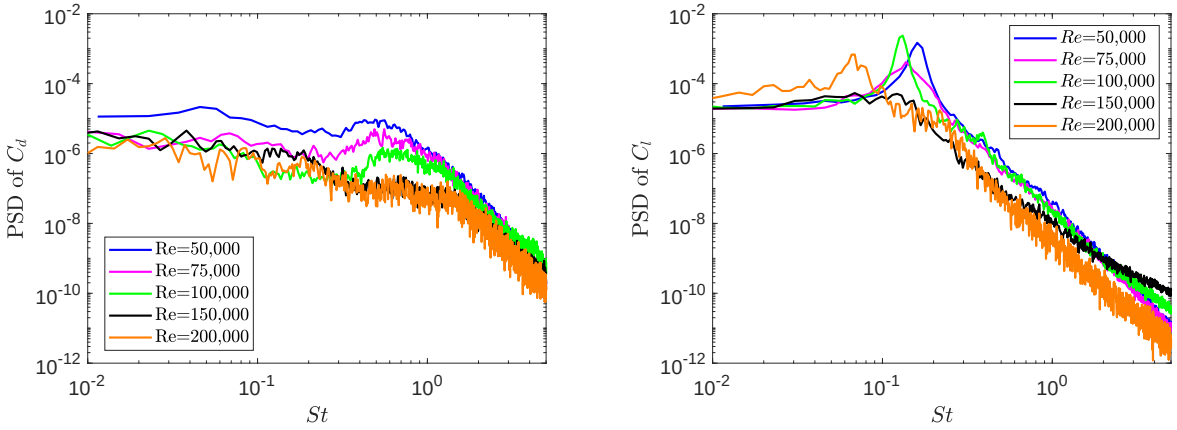

(a) PSDs of C_d for $R/L = 1/12$

(b) PSDs of C_l for $R/L = 2/5$

Figure 10: PSDs of the aerodynamic coefficients at different Reynolds numbers

In summary, force coefficients are affected by both the corner radius and the Reynolds number, while their rms values are much more sensitive than the mean drag coefficient. In addition, the value of $C_{l,\mathrm{rms}}$ is higher than $C_{d,\mathrm{rms}}$ for all cases considered. The mean drag coefficient and the rms values of the aerodynamic coefficients do not change monotonically with the increase of the corner radius. The value of $\overline{C}_d$ drops significantly once the sharp corners of the cube are rounded and the lowest value is observed for $R/L = 1/3$. Larger values of $C_{d,\mathrm{rms}}$ and $C_{l,\mathrm{rms}}$ are observed for $R/L = 0$ and 2/5. These large fluctuations observed in $C_{l,\mathrm{rms}}$, especially for the case with $R/L = 2/5$, are closely related to periodic shedding in the wake. However, no systematic dependence of these force coefficients on the Reynolds number is found. More explanations about the observed trends of aerodynamic coefficients and their relation to the flow field are presented in Section 5.5.

5.2. Flow patterns around cubes with rounded corners

5.2.1. Visualization of flow structures

Three-dimensional flow structures around cubes with different corner radii at the Reynolds number of $50,000$ are visualised in Fig. 11 based on the Q-criterion [63]. This illustrates the iso-surface of the instantaneous vortices at the normalised $Q_n = Q/(U_\infty/L)^2 = 1$, which are coloured by the mean streamwise velocity. As can be seen from Fig. 11, the flow patterns change noticeably with the variation of the corner radius. The flow separates from the leading edge for the cube with sharp corners ($R/L = 0$). With the increase of the corner radius, the separation position moves gradually downstream. As R/L is increased from 0 to 2/5, the separated shear layer moves closer to the side surfaces and the wake formed behind becomes narrower. However, the shear layer becomes more deflected again for the sphere.

Time-averaged streamlines in the $z = 0$ plane are shown in Fig. 12 together with the contours of the pressure coefficient (C_p); these are shown for different corner radii at $Re = 50,000$. Due to the symmetry of the geometry, only streamlines around the upper part of the rounded cubes are shown in Fig. 12. Flow features observed near all four side surfaces are the same, and these four surfaces are referred to as lateral surfaces in the following descriptions. The thick white line in Fig. 12 denotes locations of zero streamwise velocity, which helps to visualise positions of flow separation, reattachment and also the recirculation length in the wake. As can be seen, mean flow features around the rounded cube change significantly with the corner radius. The location of the flow separation moves downstream and the recirculation region of the separated flow above the lateral surfaces reduces in size with the increase of the corner radius from $R/L = 0$ to 2/5. In addition, the size of the recirculation region formed in the wake is also sensitive to the corner radius, and will be discussed in detail later. The secondary vortices formed near the trailing edges of the cube, highlighted in the rectangle in Fig. 12(a), disappear with the introduction of the corner radius. Similar flow features described above are also observed at other Reynolds numbers (not shown), apart from an increase in the recirculation region above the lateral surface for $R/L = 1/6$ at $Re = 200,000$. Parameters reflecting mean flow characteristics, such as the separation angle and the recirculation length, will be discussed quantitatively in Section 5.2.2.

From Fig. 12(a) for the cube, the separated flow is convected downstream and forms vortices in the wake without reattaching to the cube surfaces. Similar flow behaviour can also be observed for the sphere (Fig. 12(f)) and for R/L= 1/12 (Fig. 12(b)), although in the latter case the white line in the Fig. 12(b) is very close to the

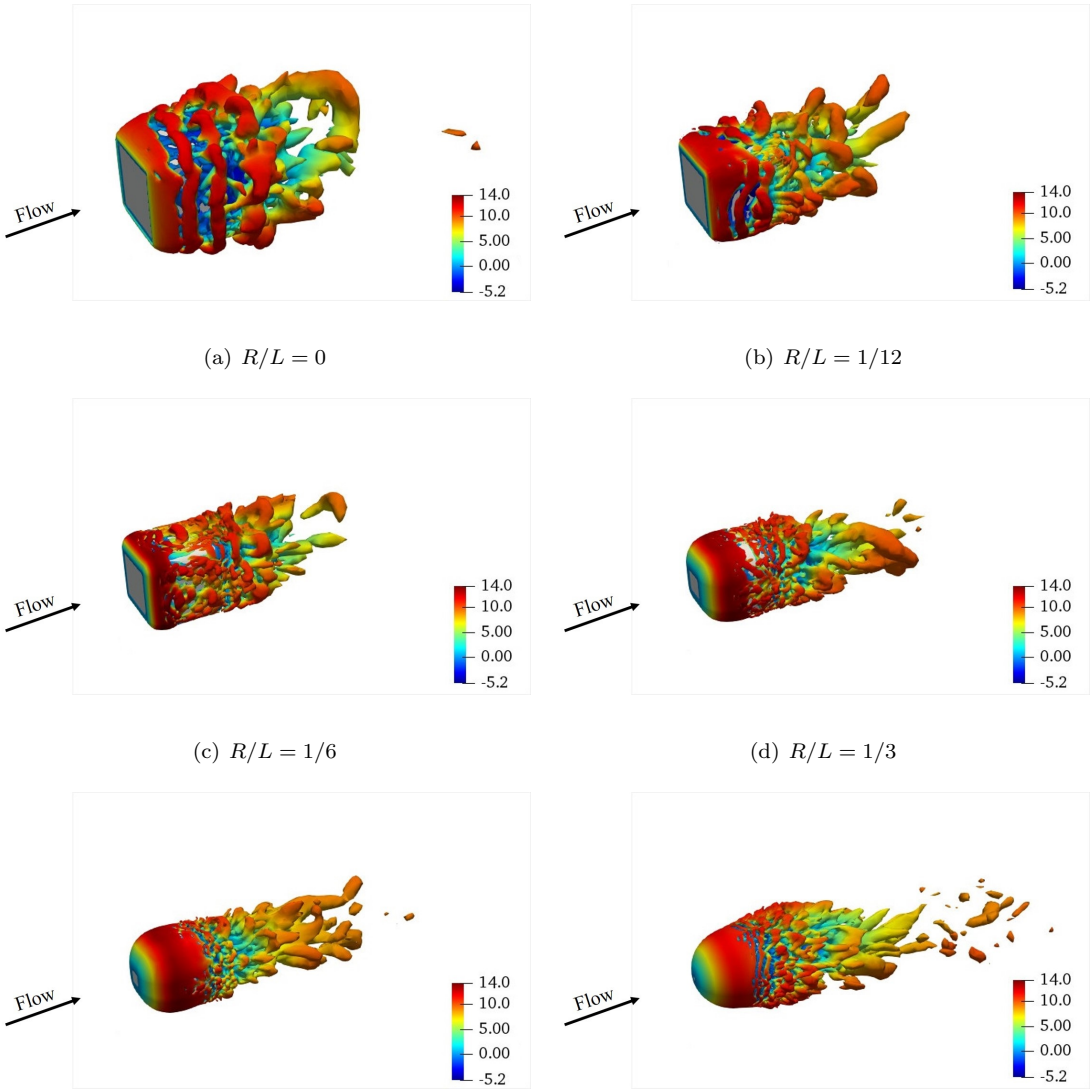

(a) $R/L = 0$ (b) $R/L = 1/12$

(c) $R/L = 1/6$ (d) $R/L = 1/3$

(e) $R/L = 2/5$ (f) $R/L = 1/2$

Figure 11: Instantaneous flow structures at $Q_n = 1$ for cubes with different corner radii at $Re = 50,000$

lateral surface. for $R/L = 1/12$ (Fig. 12(b)) and for the sphere (Fig. 12(f)). Unlike the flow around the cube, the separated flow from rounded cubes with $R/L = 1/6$, $1/3$ and $2/5$ shown in Fig. 12(c)-12(e) reattaches to the lateral surfaces before the trailing corner and then separates again from the trailing corners. Therefore, two mean flow patterns can be identified as shown in Fig. 13. The dashed line in Fig. 13 represents the developed bubble from the separated flow and θ is the separation angle measured between the upstream direction and the line linking the corner centre and the separation point. L_s and H shown in Fig. 13(b) are the length and height of the bubble formed on the lateral surfaces. A reduction in L_s always occurs together with a reduction in H. In summary, the flow around the cube and sphere at all the investigated Reynolds numbers, along with the case for $R/L = 1/12$ at

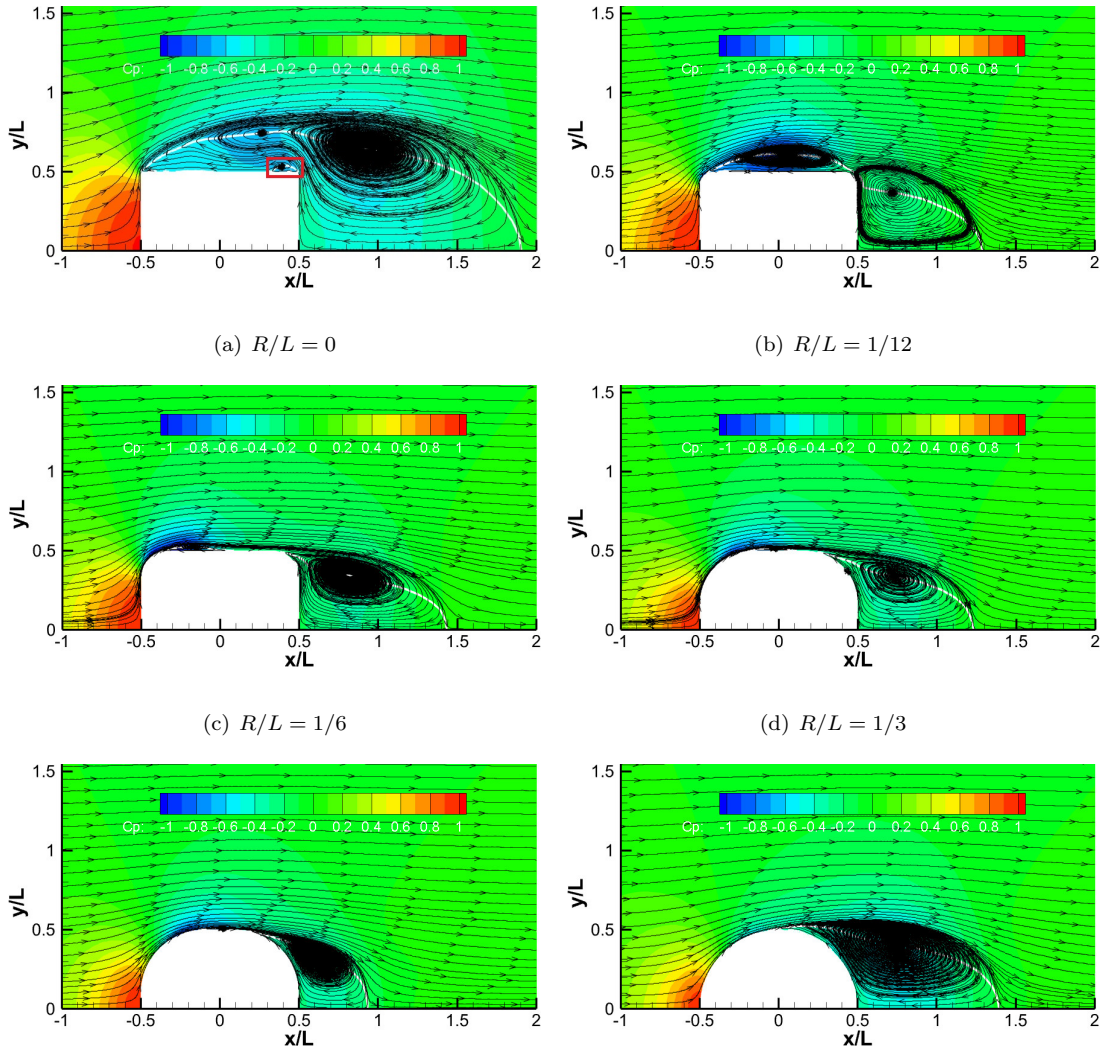

(a) $R/L = 0$ (b) $R/L = 1/12$

(c) $R/L = 1/6$ (d) $R/L = 1/3$

(e) $R/L = 2/5$ (f) $R/L = 1/2$

Figure 12: Mean streamlines and pressure contours in the $z = 0$ plane for cubes with different corner radii at $Re = 50,000$

$Re = 50,000$, follows pattern 1, while the flow induced by all the other rounded cases studied here follows pattern 2. In general, the transformation of the flow from pattern 1 to pattern 2 is facilitated by increasing the corner radius. For the second flow pattern, L_s and H tend to reduce as R is increased, although it is difficult to quantify this effect.

Fig. 14 shows the mean streamlines and the pressure contours around the rounded cube with $R/L = 1/12$ at different Reynolds numbers; the case of $Re = 50,000$ was shown in Fig. 12(b). Similar to increasing the corner radius, when the Reynolds number is increased, vortices formed due to the separated flow move closer to the lateral surfaces with a reduction in L_s and H (defined in Fig. 13). However, similar trends are not found for larger radii.

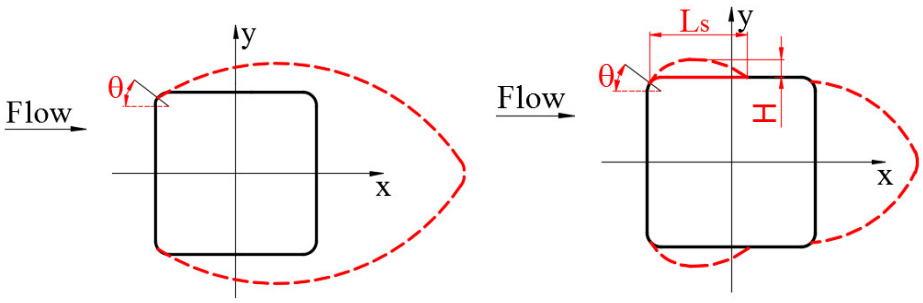

(a) Pattern 1 (b) Pattern 2

Figure 13: Flow patterns around cubes with rounded corners

For $R/L = 1/6$, the size of the recirculation region above the lateral surfaces fluctuates with the Reynolds number, while for $R/L = 1/3$ and $2/5$, the separated flow is very close to the lateral surfaces and the varying trend of L_s and H with the Reynolds number can hardly be characterised. In addition, as illustrated in Fig. 14, the size of the recirculation regions in the wake for the different cases is also dependent on the Reynolds number and more details are presented in Section 5.2.2.

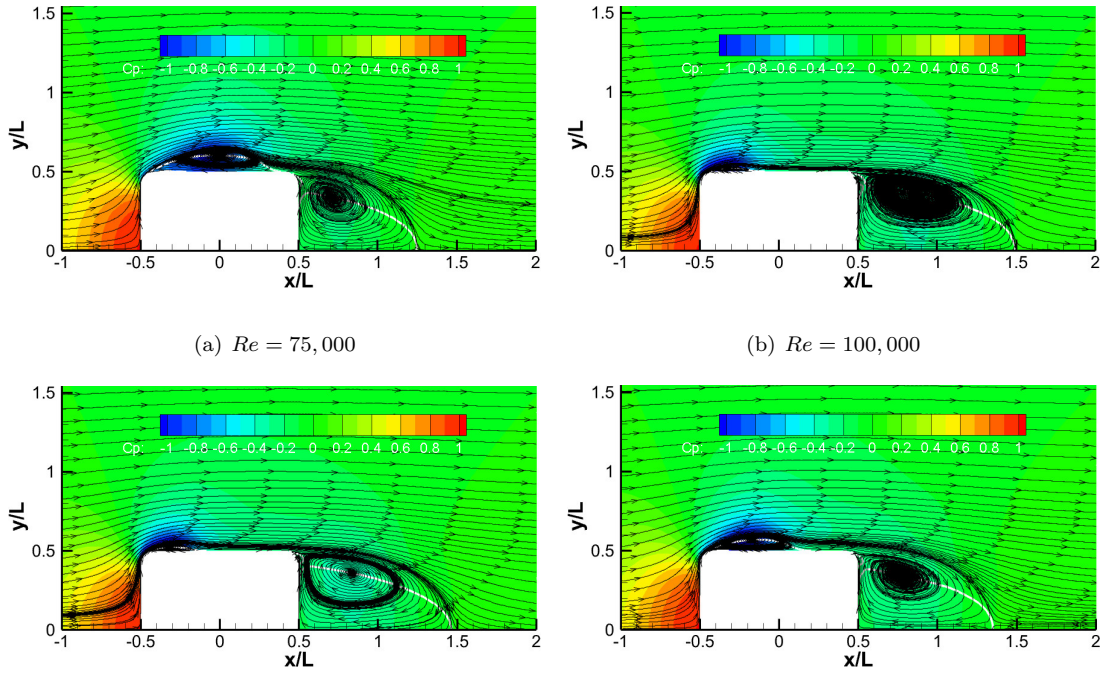

(a) $Re = 75,000$ (b) $Re = 100,000$

(c) $Re = 150,000$ (d) $Re = 200,000$

Figure 14: Mean streamlines and pressure contours in the $z = 0$ plane for the rounded cube with $R/L = 1/12$ at different Reynolds numbers

5.2.2. Locations of flow separation and the recirculation length in the wake

As discussed above, the flow separation point changes considerably with the variation of the corner radius. Similar to the determination of the separation angle in the benchmark case on the sphere described in Section 4.3, the values of θ for the rounded cubes are determined from the distribution of the skin friction coefficient (C_f). The separation angles in the $z = 0$ plane for all the investigated cases are presented in Fig. 15(a), showing the trend of the separation angle corresponding to the change of the corner radius. Since for the cube the incoming flow always separates from the leading edge, the separation angle for this case ($R/L = 0$) is assumed to be 45°. As shown in Fig. 15(a), as the corner radius increases from $R/L = 1/12$ to 2/5, the separation location moves downstream as indicated by the increased values of θ. The largest separation angle is about 85° for the case with $R/L = 2/5$, which is slightly higher than that for the sphere (82°), although the separation position for $R/L = 2/5$ is further upstream than that for the sphere. In addition, the separation angles shown in Fig. 15(a) are all smaller than 90°, which means the incoming flow always separates before it reaches the end of the leading corner. According to Fig. 15(a), the variation of θ with the Reynolds number for each radius is not monotonic. These separation angles are more sensitive to the Reynolds number for $R/L = 1/12$ and 1/6 than for larger corner radii. However, the arc lengths involved are smaller for small values of R. The flow separation is closely related with the distribution of the surface pressure, which will be discussed in Section 5.3, together with illustrations of the separation line on the cube surfaces.

The recirculation length (L_r) in the wake is measured from the rear surface to the location on the centreline ($y = 0, z = 0$) at which the mean streamwise velocity recovers from negative values to zero. As can seen from the white lines in Figs. 12 and 14, the recirculation length changes considerably with the variation of both R/L and Re. The velocity profiles in the wake of the cube along the centreline can be used to determine the values of L_r. Summaries of the recirculation length in the wake for all Reynolds numbers, including the average trend of L_r as it changes with the corner radius, are displayed in Fig. 15(b). The recirculation length reduces significantly once the cube corners are rounded with a radius of $R/L = 1/12$. With the further increase of R/L from 1/12 to 2/5, the value of L_r drops at a slower rate but it increases again for the sphere. The recirculation length in the wake is roughly inversely proportional to the base pressure coefficient (C_{pb}) [64], which is derived from the pressure directly at the back of the object and is discussed in Section 5.3. In addition, the formation of the circulation bubble in the wake of the cubes is strongly dependent on the Reynolds number, but no systematic dependence could be found for

the studied cases. The recirculation length for $R/L = 2/5$ fluctuates the most.

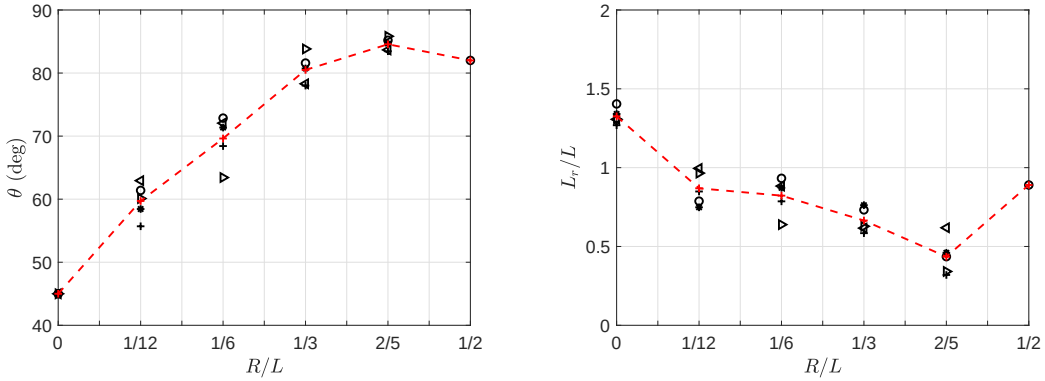

(a) Separation angle (θ)

(b) Recirculation length (L_r)

Figure 15: The trend of the separation angle (θ) and the recirculation length (L_r) varying with the corner radius (R). $\circ$: $Re = 50,000$; $*$: $Re = 75,000$; $+$: $Re = 100,000$; $\triangleleft$: $Re = 150,000$; $\triangleright$: $Re = 200,000$; $-+-$: Average value

5.3. Mean pressure distributions on the cube surfaces

The position of the flow separation is closely related to the pressure gradient along the cube surfaces since the flow separates when the adverse pressure gradient in the boundary layer is sufficient. Fig. 16 illustrates distributions of the mean pressure coefficient (C_p) for the cubes with different corner radii at $Re = 50,000$ as examples. As shown in Fig. 16, the pressure close to the leading edge of the cube drops rapidly due to the corner rounding. Consequently, the pressure on the frontal and lateral surfaces changes considerably with the increase of the corner radius. The surface pressure distributions in the $z = 0$ plane are displayed in Fig. 17(a) for different corner radii at the Reynolds number of 50,000. Fig. 17(b) shows the pressure distribution for $R/L = 1/12$ in the $z = 0$ plane at different Reynolds numbers. The pressure distributions in Fig. 17(a) and 17(b) start from the frontal stagnation point and the abscissa is the distance around the surface normalised by one quarter of the perimeter.

As can be seen from Fig. 17(a), the value of the minimum pressure coefficient ($C_{p,\min}$) changes significantly for different corner radii. The variation of $C_{p,\min}$ for all the investigated cases is summarised in Fig. 18(a). The values of $C_{p,\min}$ for cubes with rounded corners are smaller than those for the cube and the sphere. In addition, $C_{p,\min}$ becomes less sensitive to Reynolds number with the increase of the corner radius. The trends of $C_{p,\min}$ at different Reynolds numbers in Fig. 18(a) are strongly linked to those for the separation angle shown in Fig. 15(a). Large variations of $C_{p,\min}$ imply differences in pressure recovery and adverse pressure gradients, which lead to considerable

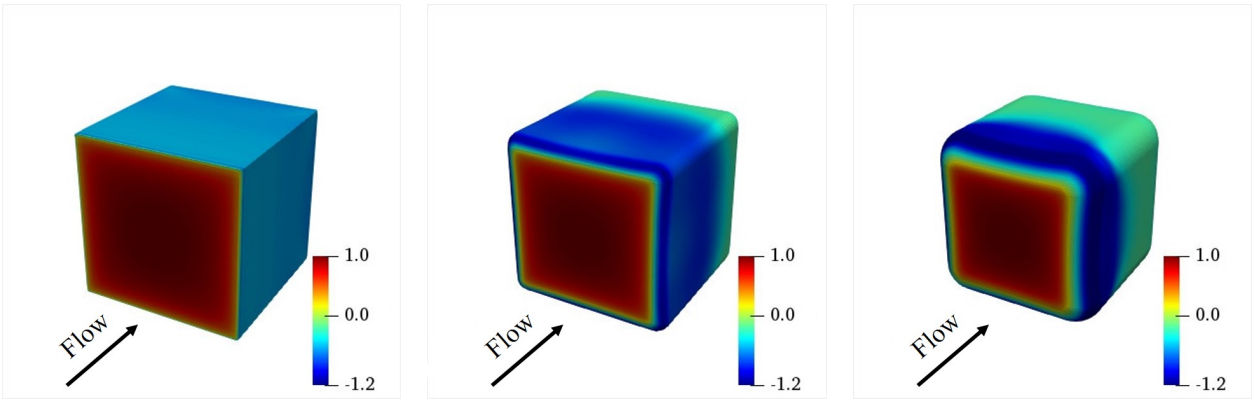

(a) $R/L = 0$ (b) $R/L = 1/12$ (c) $R/L = 1/6$

(d) $R/L = 1/3$ (e) $R/L = 2/5$ (f) $R/L = 1/2$

Figure 16: Contours of the mean pressure coefficient (C_p) on cube surfaces at $Re = 50,000$.

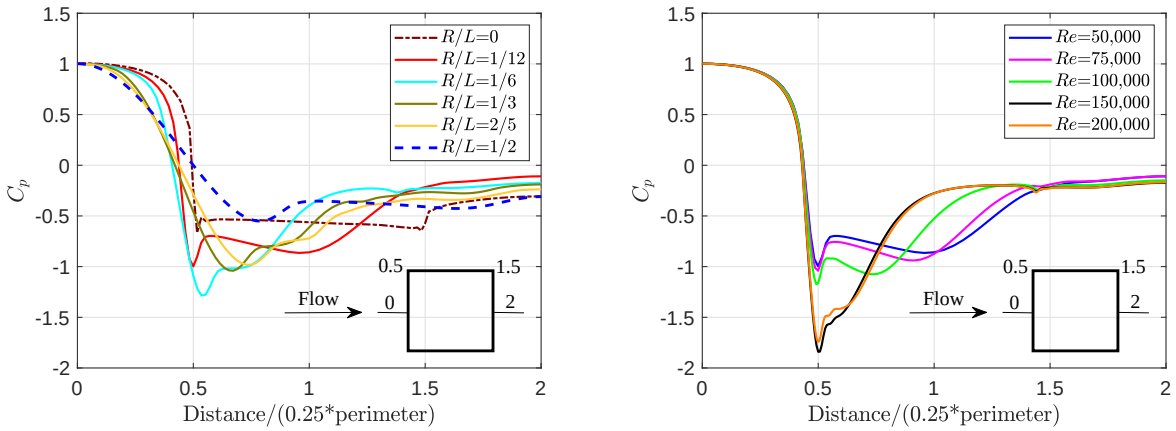

(a) $Re = 50,000$ (b) $R/L = 1/12$

Figure 17: Distributions of the mean pressure coefficient (C_p) along cube surfaces in the $z = 0$ plane.

changes of the flow separation.

With the increase of the corner radius, the position of the minimum pressure coefficient ($C_{p,\min}$) gradually moves downstream as seen in Fig. 17(a), giving a large region of favourable pressure gradient, which helps in delaying flow separation. This is consistent with the trend of the separation angle shown in Fig. 15(a), apart from the slight drop in the separation angle for the sphere. As illustrated in Fig. 17(b), the position of $C_{p,\min}$ is almost independent of the Reynolds number for the case of $R/L = 1/12$. The variations of the position of $C_{p,\min}$ at different Reynolds numbers are also very small for the other rounded cubes, as plotted in Fig. 18(b) against the corner radius. The steepest increase can be found between $R/L = 1/6$ and $1/3$. The base pressure coefficients (C_{pb}), are summarised in Fig. 18(c). $-C_{pb}$ decreases when the cube is rounded with $R/L = 1/12$, but increases as the corner radius is further increased. In addition, C_{pb} for the cubes with smaller rounded radius tends to be more affected by changes in the Reynolds number.

As shown in Fig. 17(b), the value of $C_{p,\min}$ for the cube with $R/L = 1/12$ drops significantly when Re is increased from $100,000$ to $150,000$ along with a more rapid recovery of the negative pressure. This large reduction in $C_{p,\min}$ leads to the corresponding large increase of the separation angle shown in Fig. 15(a). Consequently, the flow patterns close to the cube surfaces change considerably with Re. To identify the reasons, Fig. 19 compares the pressure contours on the lateral surface of the cube with $R/L = 1/12$ for $Re = 100,000$ and $150,000$ and also the mean streamlines obtained from the first layer of the mesh on the lateral surface. Critical points (Node and Saddle) characterising the flow topology are also labelled in Fig. 19; the definition of these points can be found in [65]. The dotted white rectangle denotes the flat part of the surface and the white solid line shows locations of zero streamwise velocity. As can be seen, with the increase of the Reynolds number from $100,000$ to $150,000$, the separation line moves downstream to reach the flat part (the dotted rectangle). A Node labelled 'N3' can be seen at $Re = 100,000$ in Fig. 19(a) and two vortices are formed beside it near the leading edge of the dotted rectangle, namely, at the end of the leading corner. However, the Node 'N3' disappears at the higher Reynolds number shown in Fig. 19(b), together with these two vortices beside it. Nodes 'N1' and 'N2' formed near the side corners move upstream as does the Saddle 'S1'.

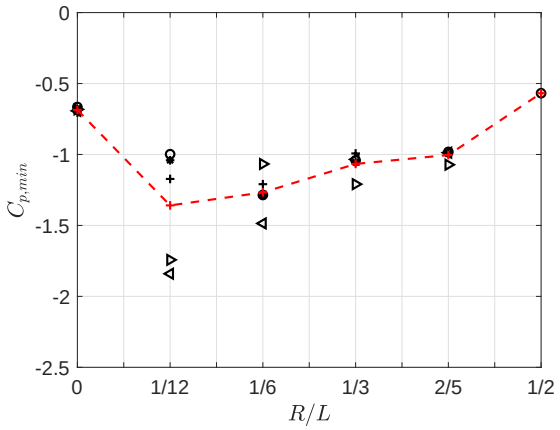

(a) Minimum pressure coefficient ($C_{p,\min}$)

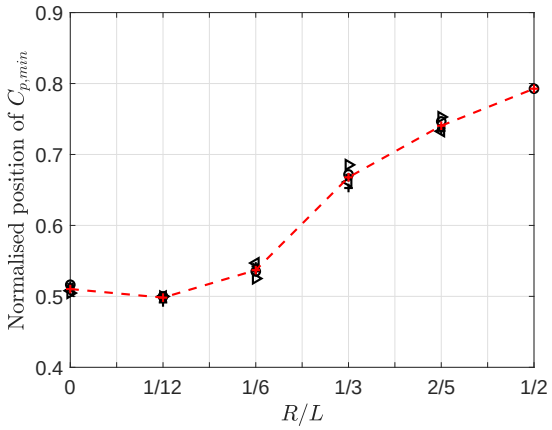

(b) Normalised position of $C_{p,\min}$

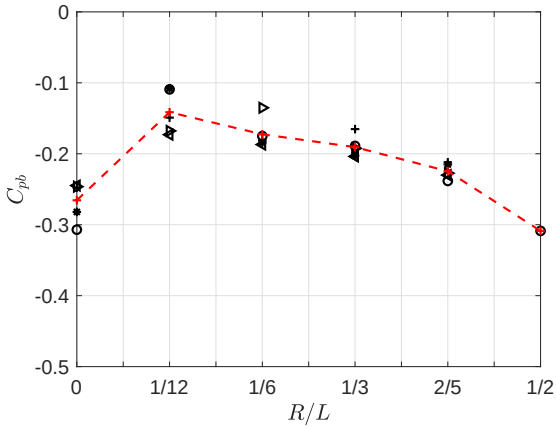

(c) Base pressure coefficient

Figure 18: Main features of the pressure distribution along cube surfaces in the $z = 0$ plane. $\circ$: $Re = 50,000$; $*$: $Re = 75,000$; $+$: $Re = 100,000$; $\triangleleft$: $Re = 150,000$; $\triangleright$: $Re = 200,000$; $-+-$: Average value

5.4. Pressure fluctuations on the cube surfaces

The pressure fluctuations on solid walls are instructive indicators for the noise prediction, since they are related with the dipole noise sources. The trends of the overall pressure fluctuations are consistent with the predicted far-field noise for the cases studied in this paper. More details can be found in reference [66]. Contours of the rms pressure fluctuations (p_{rms}) on the lateral surfaces are shown in Fig. 20 for $Re = 50,000$, together with the flow patterns represented by the time-averaged streamlines obtained from the first layer mesh beside the lateral surface. In Fig. 20, the rms values of the surface pressure are given in dB as:

$$L_p = 10\log_{10}\left(\frac{p_{\text{rms}}}{p_{\text{ref}}}\right)^2, \text{ where } p_{\text{ref}} = 2\times10^{-5}\,\text{Pa} \tag{5}$$

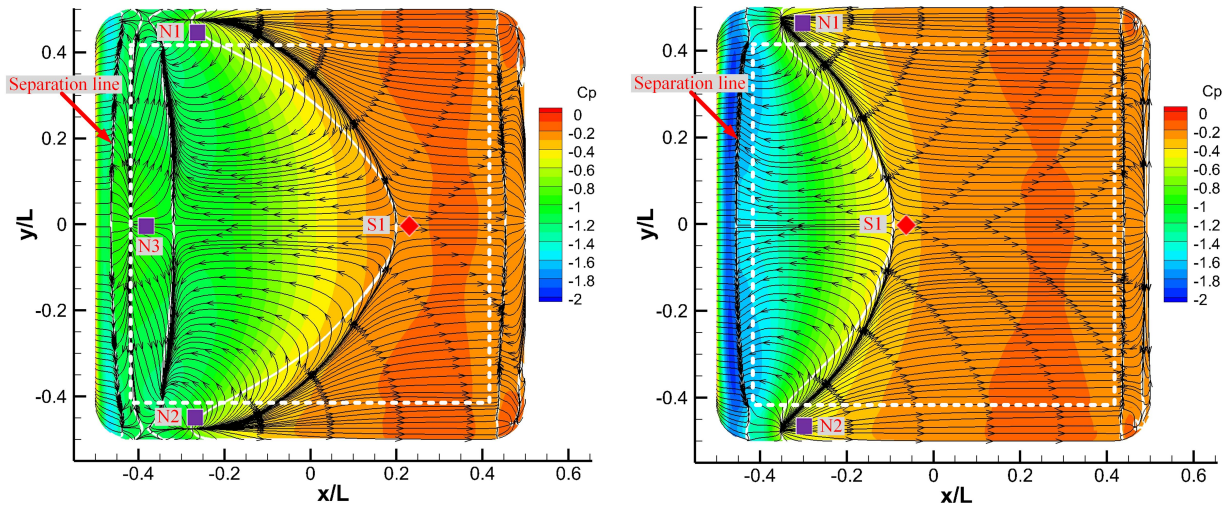

(a) $Re = 100,000$ (b) $Re = 150,000$

Figure 19: Mean streamlines and pressure contours close to the lateral surface of the cube with $R/L = 1/12$ at different Reynolds numbers (square: node; diamond: saddle)

Due to the symmetry of the objects, only the flat parts of the frontal and the rear surfaces are not shown in Fig. 20. However, the pressure fluctuations on the flat part of the frontal area caused by the flow impingement are about 35 dB lower than the highest fluctuation observed on the lateral surfaces, while those on the flat part of the rear surface are about 15 dB lower. Therefore, these parts have little influence on the radiated noise.

As can be seen from Fig. 20, the distribution of the pressure fluctuations changes significantly with the increase of the corner radius. For the cube in Fig. 20(a), the strongest pressure fluctuation occurs close to the trailing edge where the secondary vortex forms (see Fig. 12(a)), represented by Saddle 'S1' and Nodes 'N1' and 'N2'. For the case with $R/L = 1/12$ in Fig 20(b), the separated flow partially reattaches to the lateral surface with Nodes 'N4' and 'N5' appearing. The largest values of p_{rms} are found around the white lines close to Nodes 'N1' and 'N2', implying locations of flow reattachment. For larger corner radii, $R/L = 1/6$ to $2/5$, the separated flow completely reattaches to the lateral surface with a recirculation bubble being generated and high pressure fluctuations being observed inside the recirculation region, as shown in Fig. 20(c) - 20(e). The largest fluctuating pressure in the recirculation bubble close to the lateral surface is observed for $R/L = 1/6$ in Fig. 20(c). The size of the recirculation bubble reduces with further increase of the corner radius, as shown previously in Fig. 12(c) - 12(e), and so does the pressure fluctuation inside it. In addition, due to the shortened recirculation length formed in the wake of the rounded cube with larger corner radius, as shown in Fig. 15(b), the pressure fluctuations close to the rear corner

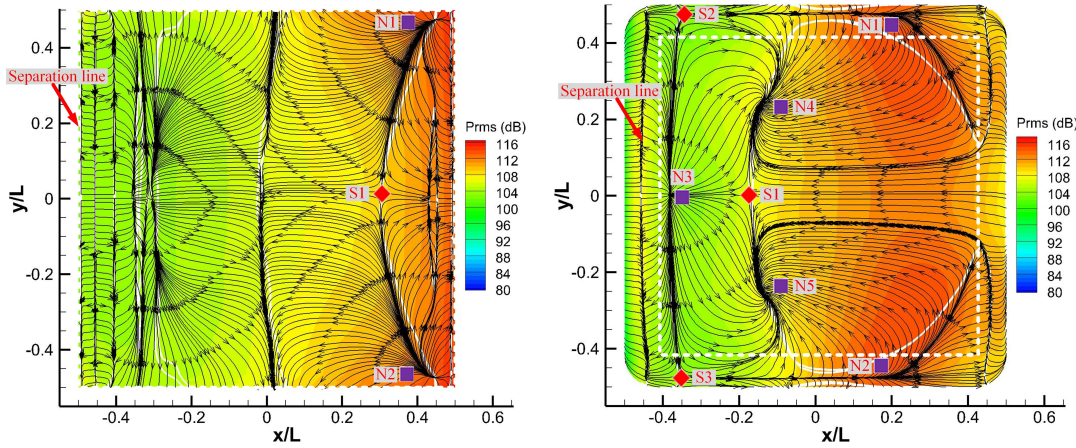

(a) $R/L = 0$

(b) $R/L = 1/12$

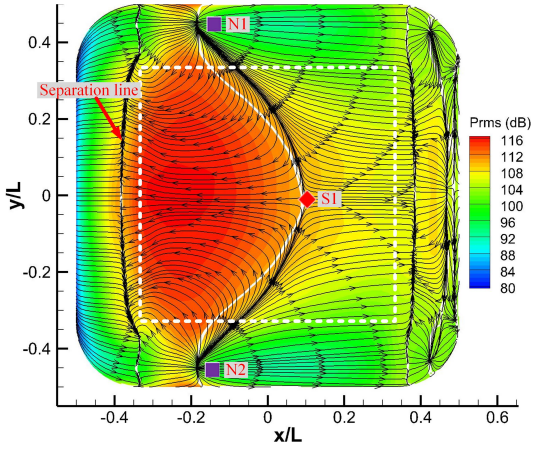

(c) $R/L = 1/6$

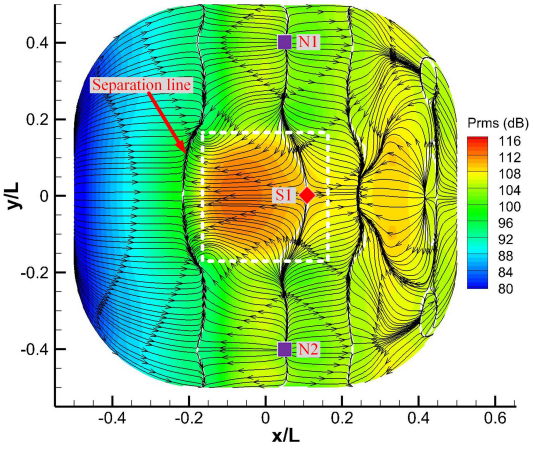

(d) $R/L = 1/3$

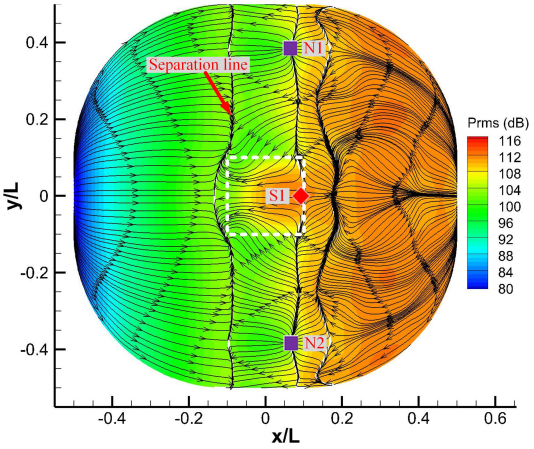

(e) $R/L = 2/5$

Figure 20: Mean streamlines and contours of pressure fluctuations on the lateral surface of cube and rounded cubes at $Re = 50,000$. (square: node; diamond: saddle; the white dotted line: flat part of the lateral surface).

increase. Generally, the relationship between flow patterns around these cubes and locations of large pressure fluctuations described above for $Re = 50,000$ is also observed at the other Reynolds numbers.

To show the effect of Reynolds number, Fig. 21 displays flow patterns and contours of the pressure fluctuation on the lateral surface for $R/L = 1/6$. Due to the similar position of the separation line, flow patterns observed in Fig. 20(c) and Fig. 21(a) - 21(c) are similar despite the different size of the recirculation region indicated by the white solid line, inside which large pressure fluctuations are observed. However, the separation line moves upstream considerably from $Re = 150,000$ to $Re = 200,000$, which is consistent with the drop in the corresponding separation angle seen in Fig. 15(a). Consequently, a Node 'N3' and two additional vortices appear close to the leading edge of the flat surface in Fig. 21(d) and the level of pressure fluctuations near this location reduces significantly. In addition, variations of the pressure fluctuation close to the rear rounded corners can also be observed in Fig. 21, which are caused by the different sizes of the recirculation region formed in the wake, as shown in Fig. 15(b). As described above, the distribution of the pressure fluctuation is strongly related to the flow structures close to the cube surfaces, which are dependent on both the corner radius and the Reynolds number. In summary, large pressure fluctuations are associated with the formation of the secondary vortex for the flow pattern 1 shown in Fig. 13(a) while the recirculation bubble, the flow reattachment on the lateral surfaces and also the shortened recirculation length in the wake are responsible for large values of p_{rms} for the flow pattern 2 in Fig. 13(b).

5.5. Relation between flow features and aerodynamic coefficients

As mentioned in Section 5.1, trends of the aerodynamic coefficients with the corner radii and Reynolds numbers are closely related with the flow behaviour. Becker et al. [67] and Kaltenbacher et al. [68] investigated the aerodynamic noise emitted from wall-mounted cylinders with different geometries. They analysed the correlation between the tonal noise and the flow field in detail. Particularly, effect of the lateral vortex on the vortex streets in the wake was studied, which is also instructive in understanding the flow physics in this paper. In addition, the reference area A in Eq. (4) also varies with the corner radius. Specifically, A can be written as follows:

$$A = (L - 2R)^2 + 4R(L - 2R) + \pi R^2 \tag{6}$$

Fig. 22 shows the reference area normalised by L^2, namely, A/L^2. The reduction rate of the reference area becomes larger for increased corner radii.

Trends of $\overline{C}_d$ for cubes with different corner radii shown in Fig. 7(a) are the overall effect of the variations of

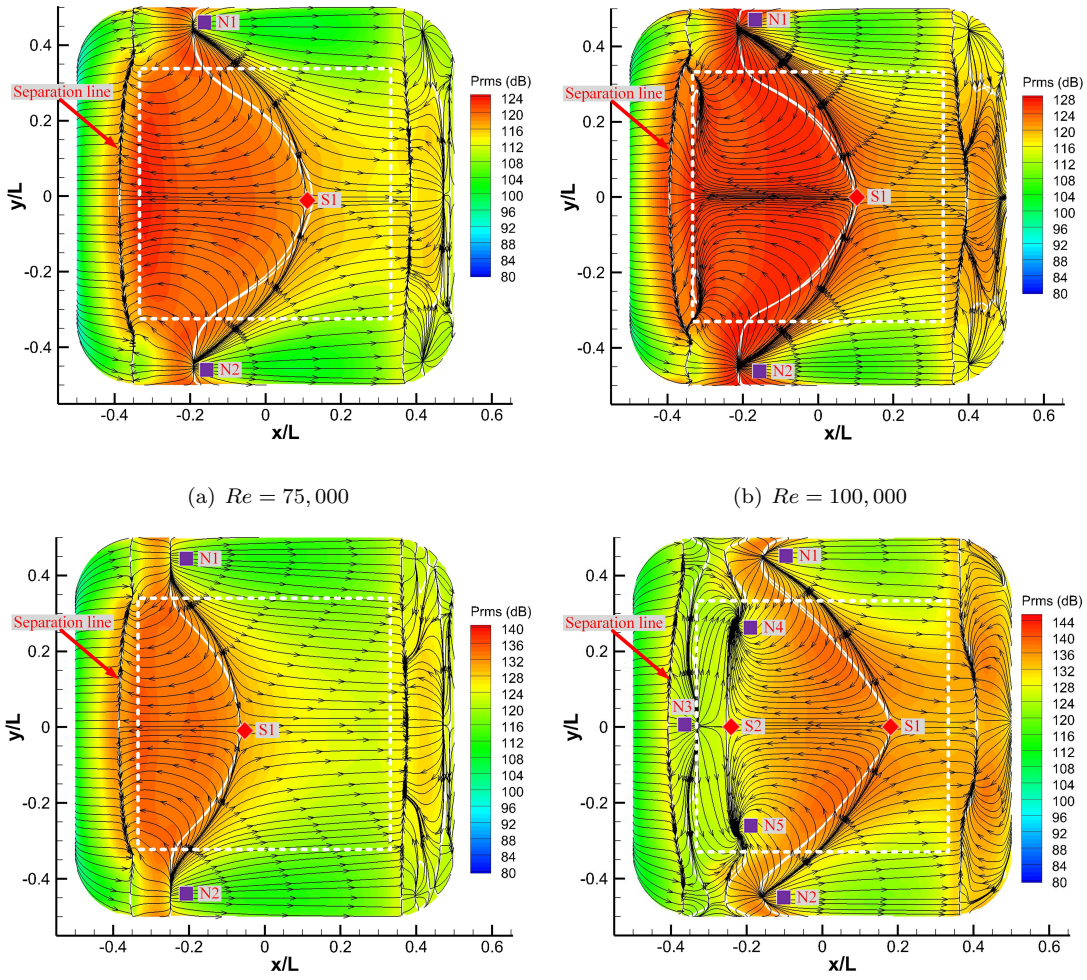

(a) $Re = 75,000$

(b) $Re = 100,000$

(c) $Re = 150,000$

(d) $Re = 200,000$

Figure 21: Mean streamlines and contours of pressure fluctuations on the lateral surface of the rounded cube with $R/L = 1/6$ at different Reynolds numbers. (square: node; diamond: saddle; the white dotted line: flat part of the lateral surface)

the surface pressure and the reference area. By rounding the cube corners, the pressure on the frontal surface close to the leading edges reduces rapidly as shown in Fig. 16. However, the base pressure for $R/L = 1/12$ becomes higher than for the cube with $R/L = 0$ as can be seen in Fig. 18(c). Therefore, the mean drag coefficient reduces considerably when a corner radius is introduced with $R/L = 1/12$. With the further increase of the corner radius, the variations of $\overline{C}_d$ becomes less significant. The decreased reference area is the main reason of the growing $\overline{C}_d$ for $R/L > 1/3$. Moreover, the flow pattern of the sphere changes to the pattern 1 shown in Fig. 13(a) while the separated flow does not reattach to the sphere surface. The surface pressure on the sphere in the separated region is higher than that for cubes with rounded corners as illustrated in Fig. 16, leading to an increased $\overline{C}_d$. In addition, the variation of $C_{p,\min}$ with the Reynolds number for each rounded cube observed in Fig. 18(a) has the same trend

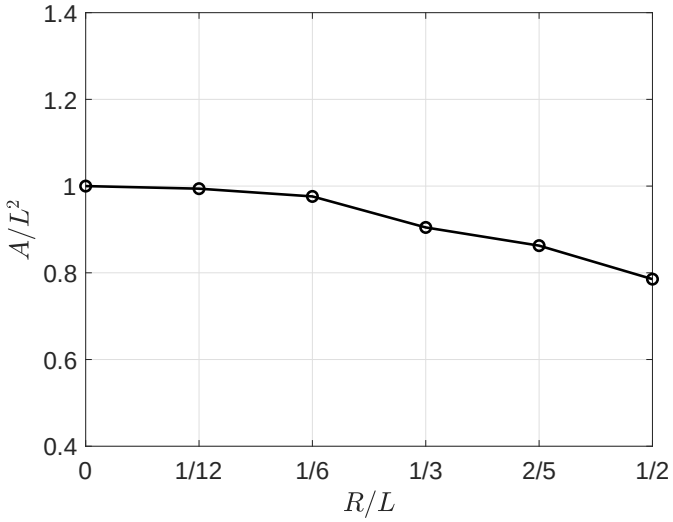

Figure 22: The reference area used to calculate the aerodynamic coefficients

as the corresponding change of the mean drag coefficient shown in Fig. 7(a). This suggests that the value of $C_{p,\min}$ is more responsible for the change in $\overline{C}_d$ than the base pressure coefficient in the cases studied here, since $C_{p,\min}$ affects the pressure distribution near the leading corner on the front surface.

As shown in Fig. 8, the rms values of the lift coefficient are always higher than $C_{d,\mathrm{rms}}$ in each case investigated. The formation of the vortex shedding in the wake of the cubes mainly contributes to the large fluctuations of $C_{l,\mathrm{rms}}$ in Fig. 8(b), which can be identified from the peaks in the PSDs shown in Figs. 9(b) and 10(b). The flow reattachment on the lateral surfaces illustrated in Fig. 12 is of great importance in the form of the vortex shedding. With the increase of the corner radius from $R/L = 0$ to $2/5$, the lateral vortices get closer to the cube surfaces, leading to less flow interactions from the side of the cube to the wake. In addition, the size of the separated region also affects the peak frequencies in the PSD spectra [67].

6. Noise from cubes with rounded corners

At low Mach numbers, the noise emitted from flow over a rigid solid body is dominated by the dipole sources, associated with the fluctuating surface pressure [69]. The highest Mach number studied here is less than 0.12; therefore, only dipole sources are considered in the noise prediction. The fluctuating pressure on the cube surfaces is obtained from the CFD simulations, and the far-field noise is predicted using the FW-H acoustic analogy (Equation (3)) in the commercial software FLUENT [70]. Although the acoustic pressure component contributing to the

pressure (p') in the FW-H analogy is not resolved in the incompressible flow solver, in the near field, especially on the solid surfaces, the hydrodynamic pressure is entirely dominant [71]. Since the free-space Green's function embedded in FLUENT is used, rather than the geometry-tailored Green's function, the noise scattering phenomenon is not considered in this work.

The far-field noise is obtained at 10 m ($133L$) from the centre of the cube at different receivers. Similar to the PSDs of the force coefficients, the noise spectra do not contain strong tonal components. Therefore 1/3 octave spectra are used as they allow the different results to be distinguished more clearly and quantifiably. Fig. 23 shows the 1/3 octave band spectra of the predicted noise at (10, 0, 0) in the streamwise direction and (0, 10, 0) in the cross-flow direction for cubes with rounded corners at $Re = 200,000$. The sound pressure level (SPL) in the frequency domain changes considerably as the corner radius is varied and is also affected by the position of the receivers. Compared with the noise spectrum for the cube $R/L = 0$, the sound for $R/L = 1/12$ and 1/6 drops by up to about 10 dB for frequencies lower than $St = 0.6$ and the highest noise level is observed close to $St = 1$. However, for the cubes with larger corner radii ($R/L = 1/3$ and 2/5), the highest sound level occurs at frequencies lower than $St = 0.6$ and the noise at Strouhal numbers greater than 1 decreases rapidly with increasing frequency. In general, the noise levels at Strouhal numbers less than 0.6 observed to the side of the cube at (0, 10, 0) are higher than those downstream at (10, 0, 0), while the opposite trend occurs for $St \geq 1$.

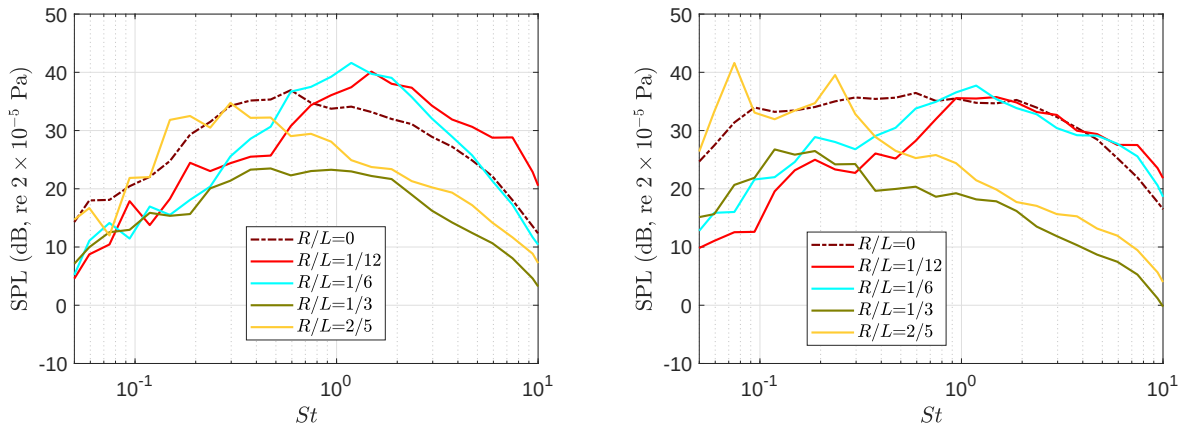

(a) Receiver (10, 0, 0)

(b) Receiver (0, 10, 0)

Figure 23: 1/3 octave band sound pressure spectra for rounded cubes at $Re = 200,000$

The SPL at $St = 10$ is around 20 dB or more lower than the maximum level of the spectrum for each case. This is also the case for the other Reynolds numbers studied. Consequently, the OASPL can be calculated by integrating

the noise PSD up to a Strouhal number of 10. Fig. 24 shows the speed dependence of the OASPL at (10, 0, 0) and (0, 10, 0) for different corner radii. As can be seen, the far-field noise grows at a rate close to $60\log U_\infty$, especially the sound from the cube. Based on the sixth power law of the flow speed observed in Fig. 24, the OASPLs at (10, 0, 0) and (0, 10, 0) at different flow speeds are corrected to 40 m/s ($Re = 200,000$) and compared in Fig. 25. As the corner radius is increased from $R/L = 1/12$ to $1/3$, the noise emitted to the far field decreases at both receivers. Although the minimum $\overline{C}_d$ is also observed for the $R/L = 1/3$, the reduction of drag does not necessarily lead to lower emitted noise [67]. This decrease of the OASPL is due to the delay in flow separation, which results in much smaller recirculating flow regions beside the cube, leading to lower pressure fluctuations. However, the sound level increases when the corner radius is further increased to $R/L = 2/5$, due to the vortex shedding in the wake. At this corner radius, despite having the smallest recirculation bubbles close to lateral surfaces of the cube, large pressure fluctuations appear near the cube trailing edge due to the reduced recirculation region in the wake. Although the sound pressure levels are corrected to correspond to the same flow speed, large differences are found between the OASPL calculated at $U_\infty = 40$ m/s ($Re = 200,000$) and that corrected from other flow speeds. In summary, the sound emitted from cubes with different corner radii approximately follows the sixth power law of the flow speed. Increasing the corner radius in the range from $R/L = 1/12$ to $1/3$ is an effective way to mitigate the far-field noise. However, with the further increase of the corner radius, the emitted noise may increase again.

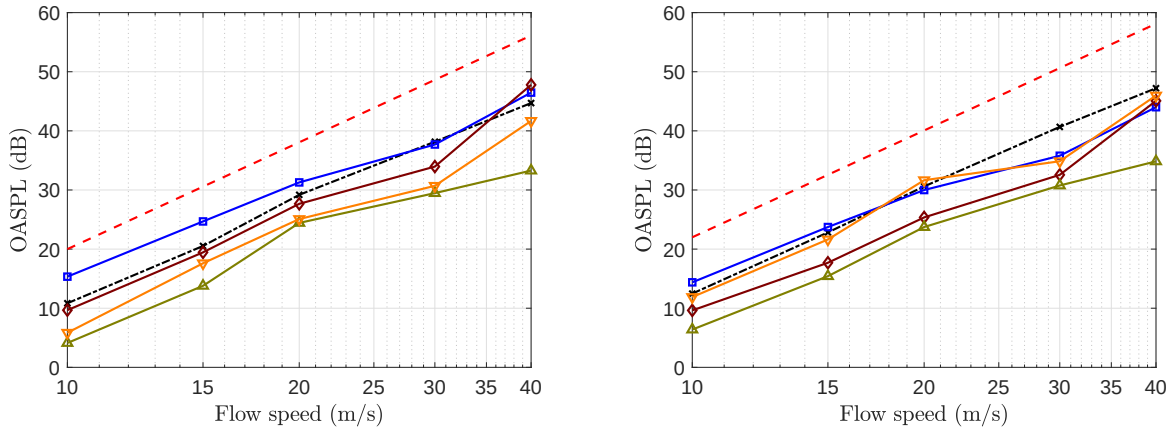

(a) Receiver (10, 0, 0)

(b) Receiver (0, 10, 0)

Figure 24: Speed dependence of the OASPL. -·×·-: $R/L = 0$; —□—: $R/L = 1/12$; —◇—: $R/L = 1/6$; —△—: $R/L = 1/3$; —▽—: $R/L = 2/5$; - - -: $60\log U_\infty$

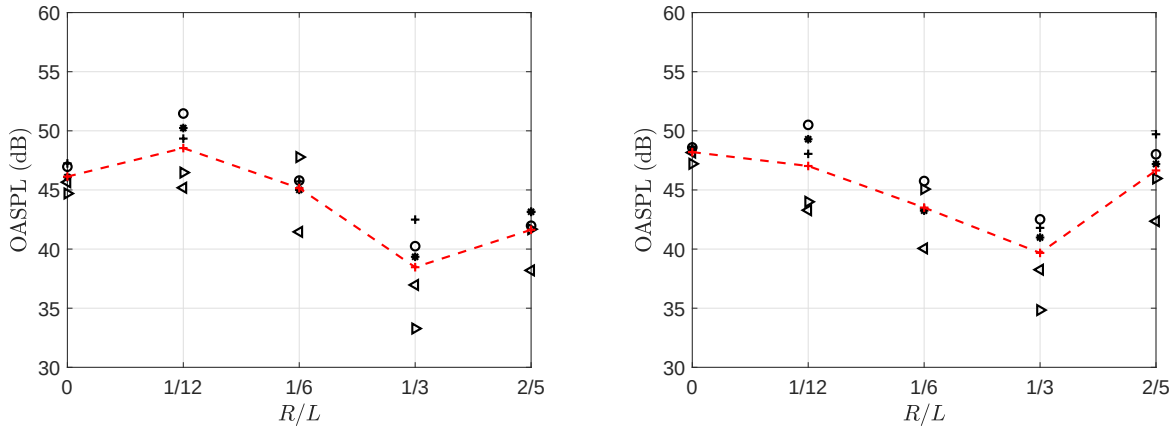

(a) Receiver (10, 0, 0)

(b) Receiver (0, 10, 0)

Figure 25: OASPL at the streamwise and the cross-flow receivers corrected to be at $Re = 200,000$. $\circ$: $Re = 50,000$; $*$: $Re = 75,000$; $+$: $Re = 100,000$; $\triangleleft$: $Re = 150,000$; $\triangleright$: $Re = 200,000$; $-+-$: Average value

7. Conclusions

The flow past cubes with rounded corners is investigated numerically and the noise emitted to the far field is also examined. A benchmark case on the flow past a sphere is first compared with available results in the literature to validate the adopted numerical methodology. Subsequently, simulations on cubes with rounded corners ranging from $R/L = 0$ to $2/5$ at Reynolds numbers from 50,000 to 200,000 are presented. The DDES approach is adopted to investigate the flow characteristics. Based on the fluctuating pressure sampled from the CFD, the far-field noise is then predicted using the FW-H acoustic analogy.

The mean drag coefficient drops significantly once the cube is rounded even with a small $R/L = 1/12$. However, its value does not change monotonically with the increase of the corner radius and the lowest value is observed for $R/L = 1/3$. The variation of the minimum pressure coefficient ($C_{p,\min}$) is found to be more related to the change of the mean drag coefficient than that of the base pressure coefficient. The rms values of the drag and the lift coefficients are more dependent on R/L and Re than the mean values and $C_{l,\mathrm{rms}}$ is always higher than $C_{d,\mathrm{rms}}$. Periodic vortex shedding is more evident in the wake of the rounded cube with $R/L = 2/5$, leading to large values of $C_{l,\mathrm{rms}}$ and significant fluctuations. Flow patterns around the cubes change significantly with the variation of both the corner radius and the Reynolds number. In general, the separation point at the leading corner moves downstream with the increase of the radius, while the separated bubble moves closer to the lateral surfaces and the recirculation length formed in the wake reduces. The distribution of pressure fluctuations is strongly related with

the near-wall flow patterns. A decreased size of the recirculation region in the wake and the flow reattachment on the lateral surface can cause large pressure fluctuations.

The emitted noise increases with the sixth power of the flow speed. The introduction of the rounded corners changes the shape of the noise spectrum. The emitted noise is reduced significantly with the increase of the corner radius from $R/L = 1/12$ to $1/3$, but the sound level increases again for a further increase in corner radius to $R/L = 2/5$ due to vortex shedding. This implies that corner rounding may be an effective way to mitigate the noise emitted from a cube, although care is needed in determining the appropriate corner radius.

Acknowledgments

This research was supported by the University of Southampton and China Scholarship Council (CSC). The simulations in this paper were carried out on the iridis 4 supercomputer at the University of Southampton.

References

[1] L. Klotz, S. Goujon-Durand, J. Rokicki, J. Wesfreid, Experimental investigation of flow behind a cube for moderate Reynolds numbers, Journal of Fluid Mechanics 750 (2014) 73–98.

[2] S. Depardon, J. Lasserre, J. Boueilh, L. Brizzi, J. Borée, Skin friction pattern analysis using near-wall PIV, Experiments in Fluids 39 (5) (2005) 805–818.

[3] A. Roshko, Experiments on the flow past a circular cylinder at very high Reynolds number, Journal of Fluid Mechanics 10 (3) (1961) 345–356.

[4] M. Breuer, Large eddy simulation of the subcritical flow past a circular cylinder: numerical and modeling aspects, International Journal for Numerical Methods in Fluids 28 (9) (1998) 1281–1302.

[5] A. Sohankar, C. Norberg, L. Davidson, Low-Reynolds-number flow around a square cylinder at incidence: study of blockage, onset of vortex shedding and outlet boundary condition, International Journal for Numerical Methods in Fluids 26 (1) (1998) 39–56.

[6] M. Breuer, J. Bernsdorf, T. Zeiser, F. Durst, Accurate computations of the laminar flow past a square cylinder based on two different methods: lattice-boltzmann and finite-volume, International Journal of Heat and Fluid Flow 21 (2) (2000) 186–196.

[7] E. Achenbach, Experiments on the flow past spheres at very high Reynolds numbers, Journal of Fluid Mechanics 54 (3) (1972) 565–575.

[8] T. Kurita, M. Hara, H. Yamada, Y. Wakabayashi, F. Mizushima, H. Satoh, T. Shikama, Reduction of pantograph noise of high-speed trains, Journal of Mechanical Systems for Transportation and Logistics 3 (1) (2010) 63–74.

[9] D. J. Thompson, E. Latorre Iglesias, X. Liu, J. Zhu, Z. Hu, Recent developments in the prediction and control of aerodynamic noise from high-speed trains, International Journal of Rail Transportation 3 (3) (2015) 119–150.

[10] S. Miran, C. H. Sohn, Numerical study of the rounded corners effect on flow past a square cylinder, International Journal of Numerical Methods for Heat & Fluid Flow 25 (4) (2015) 686–702.

[11] S. Okamoto, N. Uemura, Effect of rounding side-corners on aerodynamic forces and turbulent wake of a cube placed on a ground plane, Experiments in Fluids 11 (1) (1991) 58–64.

[12] T. Tamura, T. Miyagi, T. Kitagishi, Numerical prediction of unsteady pressures on a square cylinder with various corner shapes, Journal of Wind Engineering and Industrial Aerodynamics 74 (1998) 531–542.

[13] T. Tamura, T. Miyagi, The effect of turbulence on aerodynamic forces on a square cylinder with various corner shapes, Journal of Wind Engineering and Industrial Aerodynamics 83 (1-3) (1999) 135–145.

[14] W. Zhang, R. Samtaney, Low-Re flow past an isolated cylinder with rounded corners, Computers & Fluids 136 (2016) 384–401.

[15] J. Hu, Y. Zhou, C. Dalton, Effects of the corner radius on the near wake of a square prism, Experiments in Fluids 40 (1) (2006) 106.

[16] R. A. Kumar, C. H. Sohn, B. L. Gowda, A PIV study of the near wake flow features of a square cylinder: influence of corner radius, Journal of Mechanical Science and Technology 29 (2) (2015) 527–541.

[17] L. Carassale, A. Freda, M. Marrè-Brunenghi, Experimental investigation on the aerodynamic behavior of square cylinders with rounded corners, Journal of Fluids and Structures 44 (2014) 195–204.

[18] X. Liu, Z. Hu, D. Thompson, V. Jurdic, Reduction of aerodynamic noise from square bars by introducing spanwise waviness, Journal of Sound and Vibration 435 (10) (2018) 323–349.

[19] E. Latorre Iglesias, D. Thompson, M. Smith, Component-based model to predict aerodynamic noise from high-speed train pantographs, Journal of Sound and Vibration 394 (2017) 280–305.

[20] B. J. Vickery, Fluctuating lift and drag on a long cylinder of square cross-section in a smooth and in a turbulent stream, Journal of Fluid Mechanics 25 (3) (1966) 481–494.

[21] H. Fujita, The characteristics of the aeolian tone radiated from two-dimensional cylinders, Fluid Dynamics Research 42 (1) (2010) 015002.

[22] S. Becker, M. Escobar, C. Hahn, I. Ali, M. Kaltenbacher, B. Basel, M. Grunewald, Experimental and numerical investigation of the flow induced noise from a forward facing step, in: 11th AIAA/CEAS Aeroacoustics Conference, 2005, p. 3006.

[23] M. Awasthi, W. J. Devenport, W. N. Alexander, S. A. Glegg, Aeroacoustics of rounded forward-facing steps: Near-field behavior, AIAA Journal 57 (3) (2018) 1237–1249.

[24] M. Awasthi, W. J. Devenport, W. N. Alexander, S. A. Glegg, Aeroacoustics of rounded forward-facing steps: Far-field behavior, AIAA Journal 57 (5) (2019) 1899–1913.

[25] M. Awasthi, Sound radiated from turbulent flow over two and three-dimensional surface discontinuities, Ph.D. thesis, Virginia Tech (2015).

[26] D. K. Kaushik, D. E. Keyes, B. F. Smith, Newton-Krylov-Schwarz methods for aerodynamics problems: compressible and incompressible flows on unstructured grids., Tech. rep., Argonne National Lab., IL (US) (1999).

[27] S. B. Pope, Turbulent flows, Cambridge Univ. Press, 2001.

[28] P. R. Spalart, S. R. Allmaras, A one equation turbulence model for aerodynamic flows, AIAA Journal 94 (1992) 439.

[29] P. Spalart, W. Jou, M. Strelets, S. Allmaras, et al., Comments on the feasibility of LES for wings, and on a hybrid RANS/LES approach, Advances in DNS/LES 1 (1997) 4–8.

[30] P. R. Spalart, S. Deck, M. Shur, K. Squires, M. K. Strelets, A. Travin, A new version of detached-eddy simulation, resistant to ambiguous grid densities, Theoretical and Computational Fluid Dynamics 20 (3) (2006) 181–195.

[31] J. Fröhlich, D. von Terzi, Hybrid LES/RANS methods for the simulation of turbulent flows, Progress in Aerospace Sciences 44 (5) (2008) 349–377.

[32] F. Menter, M. Kuntz, Adaptation of eddy-viscosity turbulence models to unsteady separated flow behind vehicles, in: The Aerodynamics of Heavy Vehicles: Trucks, Buses, and Trains, Springer, 2004, pp. 339–352.

[33] A. Travin, M. Shur, M. Strelets, P. Spalart, Physical and numerical upgrades in the detached-eddy simulation of complex turbulent flows, in: Advances in LES of complex flows, Springer, 2002, pp. 239–254.

[34] S. Parneix, P. A. Durbin, M. Behnia, Computation of 3-D turbulent boundary layers using the $v^2 - f$ model, Flow, Turbulence and Combustion 60 (1) (1998) 19–46.

[35] F.-S. Lien, G. Kalitzin, Computations of transonic flow with the $v^2 - f$ turbulence model, International Journal of Heat and Fluid Flow 22 (1) (2001) 53–61.

[36] M. Mirzaei, A. Sohankar, Numerical study of convective heat transfer and fluid flow around two side by side square cylinders using $k - \omega - \overline{v^2} - f$ turbulence model, Heat and Mass Transfer 49 (12) (2013) 1755–1769.

[37] M. Mirzaei, A. Sohankar, The evaluation of a detached eddy simulation based on the $k - \omega - \overline{v^2} - f$ model with three flow configurations, Aerospace Science and Technology 43 (2015) 199–212.

[38] N. Nguyen, P.-O. Persson, J. Peraire, RANS solutions using high order discontinuous galerkin methods, in: 45th AIAA Aerospace Sciences Meeting and Exhibit, 2007, p. 914.

[39] Y. Wang, D. Thompson, Z. Hu, Numerical investigations on the flow over cuboids with different aspect ratios and the emitted noise, Physics of Fluids 32 (2) (2020) 025103.

[40] M. J. Lighthill, On sound generated aerodynamically. i. general theory, Proceedings of the Royal Society of London A: Mathematical, Physical and Engineering Sciences 211 (1107) (1952) 564–587.

[41] M. J. Lighthill, On sound generated aerodynamically. ii. turbulence as a source of sound, Proceedings of the Royal Society of London A: Mathematical, Physical and Engineering Sciences 222 (1148) (1954) 1–32.

[42] S. Glegg, W. Devenport, Aeroacoustics of low Mach number flows: fundamentals, analysis, and measurement, Academic Press, 2017.

[43] J. E. Ffowcs Williams, D. L. Hawkings, Sound generation by turbulence and surfaces in arbitrary motion, Philosophical Transactions of the Royal Society of London. Series A, Mathematical and Physical Sciences 264 (1151) (1969) 321–342.

[44] J. Franke, C. Hirsch, A. Jensen, H. Krüs, M. Schatzmann, P. Westbury, S. Miles, J. Wisse, N. Wright, Recommendations on the use of cfd in wind engineering, in: Cost action C, Vol. 14, 2004, p. C1.

[45] Y. Wang, D. Thompson, Z. Hu, Effect of wall proximity on the flow over a cube and the implications for the noise emitted, Physics of Fluids 31 (7) (2019) 077101.

[46] R. Martinuzzi, C. Tropea, The flow around surface-mounted, prismatic obstacles placed in a fully developed channel flow (data bank contribution), Journal of Fluids Engineering 115 (1) (1993) 85–92.

[47] W. Rodi, J. Ferziger, M. Breuer, M. Pourquie, Status of large eddy simulation: results of a workshop, Transactions-American Society of Mechanical Engineers Journal of Fluids Engineering 119 (1997) 248–262.

[48] A. Yakhot, H. Liu, N. Nikitin, Turbulent flow around a wall-mounted cube: A direct numerical simulation, International Journal of Heat and Fluid Flow 27 (6) (2006) 994–1009.

[49] H. Sakamoto, H. Haniu, A study on vortex shedding from spheres in a uniform flow, Journal of Fluids Engineering 112 (4) (1990) 386–392.

[50] S. Taneda, Visual observations of the flow past a sphere at Reynolds numbers between 10^4 and 10^6, Journal of Fluid Mechanics 85 (1) (1978) 187–192.

[51] E. Achenbach, Vortex shedding from spheres, Journal of Fluid Mechanics 62 (2) (1974) 209–221.

[52] E. Achenbach, Distribution of local pressure and skin friction around a circular cylinder in cross-flow up to Re$= 5 \times 10^6$, Journal of Fluid Mechanics 34 (4) (1968) 625–639.

[53] V. Bakić, M. Schmid, B. Stanković, Experimental investigation of turbulent structures of flow around a sphere, Thermal Science 10 (2) (2006) 97–112.

[54] M. Schmidt, Grobstruktursimulation turbulenter strömungen auf unstrukturierten gittern mit einer parallelen finite-volumen-methode, Ph.D. thesis, Arbeitsbereiche Schiffbau der Techn. Univ. (2002).

[55] C. Wieselsberger, Neuere feststellungen uber die gesetze des flussigkeits und luftwiderstands, Phys. Z. 22 (1921) 321.

[56] H. Schlichting, K. Gersten, Boundary-layer theory, Springer, 2016.

[57] A. G. Tomboulides, Direct and large eddy simulation of wake flows: flow past a sphere, Ph.D. thesis, Princeton University (1993).

[58] G. Constantinescu, K. Squires, Numerical investigations of flow over a sphere in the subcritical and supercritical regimes, Physics of Fluids 16 (5) (2004) 1449–1466.

[59] I. Rodríguez, O. Lehmkuhl, R. Borrell, A. Oliva, Flow dynamics in the turbulent wake of a sphere at sub-critical Reynolds numbers, Computers & Fluids 80 (2013) 233–243.

[60] E. Robertson, V. Choudhury, S. Bhushan, D. Walters, Validation of OpenFOAM numerical methods and turbulence models for incompressible bluff body flows, Computers & Fluids 123 (2015) 122–145.

[61] P. Bearman, J. Graham, E. Obasaju, G. Drossopoulos, The influence of corner radius on the forces experienced by cylindrical bluff bodies in oscillatory flow, Applied Ocean Research 6 (2) (1984) 83–89.

[62] H. C. Lim, I. P. Castro, R. P. Hoxey, Bluff bodies in deep turbulent boundary layers: Reynolds-number issues, Journal of Fluid Mechanics 571 (2007) 97–118.

[63] V. Kolář, Vortex identification: New requirements and limitations, International Journal of Heat and Fluid Flow 28 (4) (2007) 638–652.

[64] P. Bearman, Investigation of the flow behind a two-dimensional model with a blunt trailing edge and fitted with splitter plates, Journal of Fluid Mechanics 21 (2) (1965) 241–255.

[65] J. M. Délery, Robert Legendre and Henri Werlé: toward the elucidation of three-dimensional separation, Annual Review of Fluid Mechanics 33 (1) (2001) 129–154.

[66] Y. Wang, Aerodynamic flow over cuboids and the noise generated, Ph.D. thesis, University of Southampton (2020).

[67] S. Becker, C. Hahn, M. Kaltenbacher, R. Lerch, Flow-induced sound of wall-mounted cylinders with different geometries, AIAA journal 46 (9) (2008) 2265–2281.

[68] M. Kaltenbacher, M. Escobar, S. Becker, I. Ali, Numerical simulation of flow-induced noise using LES/SAS and Lighthill's acoustic analogy, International journal for numerical methods in fluids 63 (9) (2010) 1103–1122.

[69] N. Curle, The influence of solid boundaries upon aerodynamic sound, Proceedings of the Royal Society of London. Series A. Mathematical and Physical Sciences 231 (1187) (1955) 505–514.

[70] ANSYS, Ansys FLUENT user's guide, Canonsburg, PA.

[71] Y. Khalighi, A. Mani, F. Ham, P. Moin, Prediction of sound generated by complex flows at low Mach numbers, AIAA Journal 48 (2) (2010) 306–316.